https://doi.org/10.1061/(ASCE)BE.1943-5592.0001341

Serviceability Assessment of Masonry Arch Bridges Using Digital Image Correlation Technique

Manicka Dhanasekar, Ph.D.[1,*]**; Peter Prasad**[2]**; Jigme Dorji**[3]**; Tatheer Zahra, Ph.D.**[4]

[1]Professor, School of Civil Engineering and Built Environment, Queensland University of Technology, Brisbane 4000, Queensland, Australia

[2]National Bridges & Structures Engineer, Corporate Services and Safety, Australian Rail Track Corporation, Sydney 2000, New South Wales, Australia

[3]PhD Scholar, School of Civil Engineering and Built Environment, Queensland University of Technology, Brisbane 4000, Queensland, Australia

[4]Associate Lecturer, School of Civil Engineering and Built Environment, Queensland University of Technology, Brisbane 4000, Queensland, Australia

ABSTRACT

Serviceability deflections and strains at crown, support and quarter point of two aged masonry arch bridges under operating passenger and freight trains have been assessed using a digital image correlation method. Three lasers recorded the passage of the wheels; these data have been used to ascertain the wheel positions, which corresponded well with the peaks of the deflections measured. The measured maximum deflection and strain were 0.5mm and 110microstrain respectively; these data have been validated through a 3D finite element model incorporating saturated soil fill, masonry arch and their interface. The predicted strains have matched well with the field measurements. The variation of the strains to the wheel positions over the arch barrel has also been simulated. The magnitudes of the deflection and strain are quite small to cause serviceability limit state exceedance alarms for the masonry arches.

Keywords: Masonry arch; Railway bridge; Digital image correlation (DIC); Field testing; Radial strain; Tangential strain; Deflection; Arch – infill finite element modelling

---

[*] ***Corresponding Author:*** Prof. M. Dhanasekar, School of Civil Engineering and Built Environment, Queensland University of Technology, Brisbane 4000, Queensland, Australia. Ph. +61 7 3138 6666; email: m.dhanasekar@qut.edu.au

INTRODUCTION

Masonry arch bridges are one of the oldest railway infrastructure that service the rail industry even in modern times. Despite their age, these bridges are sturdy, elegant and service the society and the industry with minimal maintenance. Lack of education and research in structural masonry, the loss of skilled masons to construct these arches and the emergence of modern materials after post-war industrialisation cause concern on the safety and serviceability of these bridges to the asset owners. Decommissioning existing masonry arch bridges is a huge question as it imposes significant economic, societal and environmental costs. Many of these arch bridges in Australia have been constructed 100+ years ago for lighter loads, and lower traffic speed and volume; visual inspections have shown no cause for alarm. Therefore, with a view to proactively evaluating their ability to service the current levels of axle loads (~25T), train speeds (up to 160km/h) and volume (~30MGT), one arch in two masonry rail bridges have been identified for deflection and strain measurement.

Many theoretical methods are readily available to assess the collapse load and the reliability and safety factors of masonry arches using the ultimate load conditions. Military Engineering Experimental Establishment (MEXE) method (Harvey 1998), 2D mechanism method models such as Ring-3, Archie-M and Elasto-plastic models that incorporate the geometry of the arch bridge and assumption on the material properties (Audenaert and Beke 2010) are some of the simple, yet highly conservative methods. On the other hand, more sophisticated finite element analysis models require rigorous and complex modelling; reliable input parameters consistent with the existing conditions is often a challenge for the use of FE methods.

Contrary to the ultimate load and safety analysis, theoretical models for the assessment of the serviceability of masonry arch bridges are not readily available; serviceability assessment is difficult because of the composite nature of the interacting fill material (Callaway et al. 2012), composite nature of the masonry material (Zahra and Dhanasekar 2016, Dhanasekar et al. 2017), structural shape, and the loading pattern of the train wheels (Ling et al. 2018). Rapid and less expensive visual inspections for visible cracks/ sags are often performed to assess the integrity of the arches. Detailed assessment of serviceability requires scientific determination of the deflection, strains and crack widths in the structural masonry arch under the operational loads; field testing is the best possible approach for evaluating these structural response parameters.

Contact sensors such as the linear variable differential transducers (LVDTs) and strain gauges are widely used to measure deflection and strain respectively of the rail track and bridges (Askarinejad et al., 2013; Srinivas et al., 2014, Jamtsho and Dhanasekar 2013, Kishen et al., 2013, and Dhanasekar and Bayissa, (2011a, 2011b)); installation of these sensors require extensive preparation – therefore, labour intensive and expensive. These sensors only predict the state of deflection/ strain at the point where they are attached. In contrast, the emerging non-contact digital Image Correlation (DIC) technique offers an inexpensive yet a versatile optical solution that allows determination of surface deflection and strain distribution over a range of points covered by the image. While DIC is limited to the characterisation of surface strains/ deflection, ground penetrating radar (GPR) – another optic based method – can provide information on subsurface defects (Alani et al. 2013).

There are many non-contact and non-destructive testing methods available in the literature to assess the conditions of bridges and rail tracks. Papaelias et al (2008) has provided an extensive review of these methods and techniques to detect internal fatigue damages in railheads and rail foot; Murray et al (2014) have deployed DIC to measure deflection and strains in rails under operating train loads. The condition of sleepers (cross-ties) and ballast bed has been examined using DIC by Sabato and Niezrecki (2017); the effect of ballast condition on rail joints have been examined using spatial and image analyses by Zong et al (2013). The stresses at a very localised wheel-rail interface under moving full scale wheels in the laboratory condition was examined using a 18MP camera fitted with a telescopic micro lens by Bandula-Heva et al (2013), Zong and Dhanasekar (2014) and Bandula-Heva and Dhanasekar (2014).

Steel bridges have been widely examined using DIC. Lee et al. (2006) used a telescopic lens to measure the deflection of steel bridge girder under operating train loads from a distance of 200mm and verified the results using strain gauge readings. Malesa et al. (2010) employed DIC technology to measure the deflection at mid span of a truss bridge and recorded a maximum deflection of 2.5mm under the passage of the trains. Busca et al. (2014) compared three algorithms of vision based methods to process images taken from a single camera covering the whole 50m span of a simply supported steel railway bridge and concluded the zoom and resolution levels are more important than the algorithm; a maximum midspan deflection of 8mm was detected.

As the accuracy of the DIC method depends on the quality of the images, it is essential to avoid optical interferences during imaging. For a steel bridge, Ribeiro et al. (2014) examined the factors that affect the DIC output results including lighting level, camera movement, lens magnification types and distance to the target. They concluded that camera movement and distance to the target were the most influencing factors for the DIC measurements; the error was found to increase with the magnitude of camera movement and the distance to the target larger than 5m for the type of camera/ lens combination they used. The distance between the camera and the target surface for imaging must be decided based on the optical equipment, site condition and the purpose of the study (global structural movement as in Busca et al (2014) and Feng et al (2015) or local strain distribution as in this paper). The maximum deflection recorded by them was 2.5mm for the steel girder under high speed trains (180km/hr).

Although frames can be snipped from the video camera images, higher accuracy for the local deflection and strain analysis can only be achieved using images taken from stationery cameras with the required zoom/ wide angle lenses. Malesa et al. (2010) mentioned an error of 0.1px – however, the basis of the assumption was not clarified. While monochrome images are preferred for better accuracy of determination of deflections and strains, research on the use of colour cameras (due to their common availability and economy) for bridge monitoring is on the rise (Forsey and Gungor, 2016; Li et al., 2017; Baldi, 2018) for 2D and 3D applications.

The target object must be well illuminated and the frequency of imaging (frames per second) must be greater than the frequency of the wheel passage over sleepers to ensure capturing of all peaks. Feng et al. (2015) carefully examined the parameters that affect the image based measurements of bridges, such as the ground vibration, tilt angle and non-uniform air temperature between camera and the target bridge; the authors proposed scaling factors to account for these parameters. The accuracy of results is shown to be affected by the image resolution, lighting level and the focal length of the lens by Pan et al. 2009.

DIC tracks the texture (i.e. the spatial variation of brightness) of the two successive images recorded before and after loading and use them in the determination of deflection/ strain. The images are divided into a mesh of test facets. White et al, (2003) and Thamboo et al, (2013a, b) have reported algorithms for computing the coordinates of the midpoint of each facet on each image in a series. The displaced location of each facet is evaluated from the correlation between the ‘reference’ facet extracted from “initial image” and a ‘displaced’ facet from the same part of the “successive image”. This operation is repeated for the entire mesh of facets created within the reference image and then for each successive image of a test (one test per train passage). The facet deflections are then used to determine the lateral strains, axial strains and shear strains at the intersection of all facets within the mesh of all the images.

Although there exist many publications on the usage of DIC in the lab testing of masonry as reported in Tung et al. 2008, Thamboo et al. 2013a & 2013b, Ghorbani et al. 2015, Ramos et al. 2015, Thamboo and Dhanasekar 2015, Zahra and Dhanasekar 2018, the employment of DIC for field testing of masonry structures particularly for masonry arch bridges is very rare. Koltsida et al. (2013) monitored a two-span masonry arch railway bridge in the UK under the passages of trains from a distance of 10m which covered the entire arch. They reported the global deflection of the arch bridge with respect to train location in pixel units. While the the authors provided a description of the global response of the bridge to train movement, they did not reported deflection in physical units. To the best of the knowledge of the authors, the work reported in this paper is the first of its kind for the measurement of deflection and strain in physical units at critical locations of masonry arch bridges under the operating train load using DIC technique – although Acikgoz et al (2018) have examined a damaged masonry arch viaduct in the UK using fibre brag gratings (FBG) and DIC (using video cameras).

This paper first presents the details of the field investigation carried out on two masonry arch bridges in Australia. It then reports the methodology of DIC analysis, followed by the results. The deflection and strains obtained from the key regions (crown, quarter point and support) have then been mapped against the wheel positions obtained from laser datasets. FE analysis of a masonry arch is presented later to validate the experimental results and conclusions drawn.

FIELD TESTING

One arch in each of two aged (100+ years old) in-service rail bridges have been tested; the description of each bridge is listed in Table 1 and the selected arches are shown in Fig. 1. Digital images of the speckled patches in three key regions (crown, support and quarter point) of one half of an arch were acquired from three independent cameras, each focussing on one of the patches from approximately 4m under the passages of 10 trains from 8PM to 1AM for two consecutive nights. The acquired data have then been analysed through DIC using *ISTRA4D* - a commercial software that provides an accuracy of 0.1 pixels (*ISTRA4D* Manual, 2016). The analysis determined the deflections and strains in the axial and the radial directions of three key regions (crown, support and quarter point) of arch. Lasers were used to record the wheel positions vertically above these three regions of the respective arches. Lasers triggered digital clocks stuck in the imaging area – one each. The digital clock display was used to synchronise the laser data with the images; a relationship between the wheel position and arch deflection was established using the data.

To maximise image quality (in order not to compromise with the accuracy of results), an arch surface of each bridge very close proximity to the installed cameras has been selected for observation. The site to position the cameras was selected by giving due consideration to the distance and the normality of imaging axis to the arch surface. The details related to camera, lens and flood light are provided in Table 2.

Three regions of interest (ROIs) – support, quarter point and crown - were selected for imaging of the two arches – one on each bridge (Fig. 2). The distance between the camera and ROIs was approximately 4m. The ROIs were cleaned well by removing debris and lime deposits to ensure plane surfaces for imaging. Each ROI was speckled using permanent markers directly unto the cleaned surface within the stencil of dimension 1.2m × 1.0m for better contrast required for the monochrome image analysis. Images of each of the ROI were acquired using a high-speed (up to 166 frames / second) monochrome camera; three cameras were, therefore, used – one for each ROI. Images were taken @ 50 frames per second. Three lasers, one each above a ROI, were installed on either side of the track to capture the train wheel passing data; when a wheel crossed a ROI section, the corresponding laser triggered a digital clock attached within the speckled ROI. Fig. 3 shows the ROIs preparation and data recording processes. The digital clock time was used to ascertain the commencement of the passage of wheels above the ROI; this later was used to synchronise the deflection measured from the image data and the wheel position data. Passages of five passenger trains (19 Tons Axle load, or TAL) and five freight trains (25TAL) for each bridge were considered in the testing.

DIC ANALYSIS

The images were analysed using a special purpose software *ISTRA4D*. From each image, for each step (0.02 sec), *ISTRA4D* determined strain states of each pixel; unfortunately it did not report the strain at each pixel location. Some pixels had poor texture/ some had been affected by the presence of either droplets of water or moving insects; these pixels provided unrealistic strains and hence considered as outliers. Statistical information (Minimum, Mean and Maximum) was output for each time step for the selected subset of pixels. The minimum and maximum strains were usually the outliers and the mean was the only acceptable measure; therefore, mean strains (tangential and radial) for the selected subset of pixels within the analysed ROI were used in the time series; the same procedure was followed to establish the deflection time-series. Fig. 4 shows the process of determination of deflection/ strain.

First, the images were scaled for the known stencils dimensions (1.2m × 1.0m); coordinates were input for scaling as shown in Fig. 4(a) at each ROI. This scaling process aided conversion of the size of pixel to a physical dimension. The area of measurement (number of pixels were chosen for calculation) was defined as shown in Fig. 4(b). For results visualisation, the reference coordinate system was defined in the next step as marked in Fig. 4(c). Contours of radial deflection, tangential strains and radial strains were plotted using the *ISTRA4D* over the ROI as shown in Fig. 4(d).

The deflection/ strain contour was further analysed to determine the effect of bending of the arch (Fig. 5). For this purpose, two small patches, one each on top and bottom of the ROI was selected as shown in Fig. 5(a) and the mean values of deflection and strain over these patches were extracted for all the analysis steps. The difference in radial strain at these top and bottom patches allowed determination of the bending moment. Typically for passenger trains 1000 images (or 20 sec) and for freight trains 3000 images (or 60 sec) were analysed; these recording durations were not fixed but was affected by the length of the trains. Recording was performed for full passage of all trains.

DIC ANALYSIS RESULTS

Each camera installed perpendicular to the surface of the respective ROI was rotated such that the tangential axis aligned with the x-axis and the radial axis aligned with the y-axis of each ROI. This rotation of the camera directly provided the tangential and radial deflections/ strains along the x and y axes respectively (without any need for coordinate transformation) as marked in Figs. 5(b) and (c).

The imported *ASCII* data from *ISTRA4D* was filtered to reduce noise using the Savitzky-Golay filter (Savitzky and Golay, 1964) coded in *MATLAB* prior to plotting the time series. This filter reduced the data oscillations and retained the positive and negative peaks. The noise level in the analysed data was determined by correlating the images of ROI with and without train traffic. The deflection of the crown of Bridge 1 free of loading is shown in Fig. 6, which shows oscillations. These oscillations (unfiltered) could not be related to the bridge response as there was no load and should have been caused by the shutter release, noise and subpixel interpolation algorithms specific to the camera. The amplitude of this noise (0.05pixels) was, therefore, treated as the uncertainty of the measurement; the maximum uncertainty determined was ±0.05mm corresponded to 0.05 pixels, which was 10 fold smaller than ±0.5mm (0.5 pixels) reported in Malesa et al. (2010). This noise level (oscillations) in the data was further reduced to ±0.025mm by applying the Savitzky-Golay filter. The measured and the filtered data are shown in Fig. 6. The details of the DIC and filter parameters are provided in Table 3.

The time series for deflection and tangential and radial strain for all the passenger and freight trains recorded from both bridges have thus been calculated.

Deflections

The radial deflection at the three ROIs on Bridge 1 under the passage of a passenger train is shown in Figs. 7(a), (b), (c) respectively. Fig. 7(d) shows the variation of deflection from crown to support; as one would expect, crown experienced the largest deflection. The maximum deflection measured was 0.1mm. The signature of radial deflection for a passenger train (not the same train passed through Bridge 1) passing the Bridge 2 is shown in Fig. 8. The maximum deflection at crown was 0.07mm – smaller than 0.1mm in Bridge 1 due to different span and shape. The maximum deflection for members under bending allowable in the Australian masonry structures standard AS3700 (2018) is span/360. The span of Bridge 1 is 9.3m, therefore, the allowable deflection is 25.8 mm which is very large compared to the 0.1mm and 0.07mm maximum deflections measured in Bridge 1 and Bridge 2 respectively.

The time series of radial deflection for freight trains (not the same train) on Bridges 1 and 2 are shown in Figs. 9 and 10 respectively. The maximum deflection recorded for Bridges 1 and 2 were 0.5mm and 0.24mm respectively; these deflections are significantly larger than those observed under passenger trains, yet is much lower than the allowable deflection of 25.8mm and hence is not a concern. The measured peak deflection was maximum at the crown and the lowest at the support. Similar signatures and trends are reported in Kishen et al. (2013), Srinivas et al. (2014) and Ataei et al. (2017). The correlation between the deflection signatures and train wheel positions is discussed in the ensuing laser data analysis section.

Tangential (Axial) Strains

The tangential strains were analysed using the recorded time frames for the three ROIs of both the bridges. The signatures were determined for the passenger and for the freight trains. The tangential strain signatures for the passenger train on Bridge 1 and 2 are presented in Figs. 11 and 12 respectively.

The measured strains were very low - maximum was 75μ for Bridge 1 and 110μ for Bridge 2 - and remained well within the elastic limits of masonry. The peak compressive strain variation is shown to gradually increase from crown to support. It is believed that the wheel positions play an important role in the trend of strain variation over the arch length (Melbourne, 2008). In addition, entrapped water in the fill material could have added to the pressure on the arch at sections below the crown. Similar strains for water logged masonry arch bridges were also reported by Orban and Gutermann (2009).

Radial Strains

The signatures of radial strains were also determined using the procedure followed for the tangential strains. Therefore, only the variation of the peak radial strains across the three key ROIs is presented in this section. Moreover, relatively higher strains were measured for Bridge 2 as shown in Fig. 13. The maximum strain of ~80μ was recorded at support for Bridge 1 (Fig. 13(a)) and 110μ was recorded at support for the freight train on Bridge 2 (Fig. 13(d)). Peak radial strains were consistently larger at support. It should be remembered that these peak strains did not correspond to a single wheel position; rather the wheel position for each of these peaks were different. The sensitivity of peak strains to wheel positions is demonstrated later under the finite element analysis section of this paper. The reason for consistently larger radial strains at support is, therefore, attributed to the geometry of the wheel consists (described in the laser data analysis section) and the shape and span of the arches examined.

LASER DATA ANALYSIS

The lasers were installed on the rail track on each ROI (crown, quarter point and support) to capture the wheel passing time series for each train. The laser signals dropped when the wheel crossed the track (obstructing the laser beam) and the signal data was recorded against the installed digital clocks time. Typical plots of wheel passing laser signal for a passenger and a freight train are shown in Fig. 14(a) and (b) respectively. Using these data, the wheel positions, train speed and train length were determined.

The train length and wheel positions for a typical passenger and freight train are shown in Fig. 15. Typically passenger train was 87m long and the freight train was 595m long and their speeds were approximately 110km/h and 80km/h respectively. Each bogie (two wheelset consists) of the passenger train was spaced 13.2m within a passenger car and 5.1m between adjacent passenger cars as shown in Fig. 15(a). The locomotive of the freight car consisted of three bogies (three wheelset consists) as shown in Fig. 15(b); the distance between the front and the middle and the middle and the rear bogies were 7m and 3.4 respectively.

Fig. 16 shows the crown deflection time series for a typical passenger train. The wheel positions obtained from the laser data synchronised with the time display in the digital clock are also laid out in this figure. The dots in the figure show the positions of the wheels of the part of train passing the concerned ROI (crown). It can be seen that the first axle entered the ROI at 7.80sec and caused the onset of increase in deflection; the deflection has progressively increased following the progressive passage of subsequent wheels through the ROI. The maximum deflection occurred at 8.45sec, which aligned with the position of the wheelsets belonging to the rear bogie of the front car and the front bogie of the following car as shown in the enlarged view in Fig. 16. The difference between the time of the crossing of the first wheel through the ROI and the time at which the ROI attained maximum deflection is defined as time lag in this paper (which is 0.65 sec for this case). For subsequent passages of the wheelsets, the frequency of the ROI deflection corresponded well with the frequency of the group of rear bogie wheelsets of a leading car and the front bogie wheelsets of a following car passing through the ROI. Baring the very first wheel, all other wheels did not exhibit time lag.

Fig. 17 shows the crown deflection time series along with the corresponding wheel positions for a freight train. Similar to passenger train, it also exhibited time lag; however, the time lag was slightly larger (0.77sec) as shown in the enlarged view in Fig. 17. It is believed that the lower speed of the freight train has caused this increase in time lag as the wave propagation is independent of the load. The difference between the deflection signatures of the passenger and the freight train is that, the actual deflection caused by the locomotive is larger than that caused by the wagons of the freight train, but the whole of the passenger train caused no difference in deflection – which reflects the construct of these two trains. This shows that the deflection is a function of the wheel positions, wheel spacing and axle load whereas the time lag is a function of the train speed.

To illustrate the effect of the wheel positions on the arch, a freight train on Bridge 2 was considered because it resulted the larger deflection in the field measurement. Two instances of wheel positions were considered: (i) 15.5 sec - when the centreline of the front and middle bogies of locomotive was aligned with the centreline of crown (spacing between the bogies = 7m) and, (ii) 16.0 sec - when the centreline of the middle and rear bogies of locomotive aligned with the centreline of crown (spacing between the bogies = 3.4m). ~~These instances of locomotive wheels are shown in Table 4.~~ For these positions of locomotive wheels, the corresponding tangential compressive strains at crown, quarter point and support were searched from the analysed strain data and plotted in Fig. 18. It can be seen that at 15.5 sec, the crown registered a higher strain whist at 16sec the trend reversed, with the crown registering a lower strain. These data proves that the maximum strains can occur in either of these ROIs depending on the position of the wheel. This observation was further validated using a finite element (FE) model described in the following section.

FE ANALYSIS

A three dimensional micro FE model was developed to validate the strains at the three ROIs. The geometry, meshing, boundary conditions and loading are shown in Fig. 19. ABAQUS finite element software was used for the simulation.

Model parameters

Half of the width of the bridge (4m) and half of the span of the arch (7.5m) were considered in the modelling exploiting the symmetry as shown in Fig. 19. The bridge had two (2) rail tracks of 1.435m gauge as shown in Fig. 20. The sleeper was 2.4m long and the ballast layer was 300mm thick and 3m wide. As the field strains were recorded for the trains passing on the single rail track adjacent to the arch span, to replicate the wheel loads on a single rail track using the symmetry model, two analyses were carried out: (1) with symmetric boundary constraints about z-axis and (2) with antisymmetric boundary constraints about z-axis. In each analysis, half of the wheel load was applied and the strain at the desired location from each analysis was superimposed (summed) to obtain the strain corresponding to the full load applied eccentric to the z axis (i.e., when only one track was loaded). This procedure reduced computational effort which otherwise would require several spans and full width of the bridge to fully accommodate the train.

Three locomotive wheel axles of a freight train (forming a bogie) - each 360kN Load Axle (360LA) at a spacing of 1.2m were considered as per AS5100.2 (2017). The axle load was converted to a uniformly distributed load of 120kN/m (per each axle) for a 3m width of the ballast resting on top of the arch barrel as shown in Fig. 20. Half each of this axle load (60kN/m) was applied to the symmetric and the antisymmetric models.

The actual spacing of the locomotive wheelsets limited the number of load cases that could be analysed using the x-axis symmetry exploited model. Two load cases were considered – one corresponding to 15.5 sec snapshot (7m spacing between the front and the middle bogie in Fig. 15(b)) and the other at 16.0 sec snapshot (3.4m spacing between the middle and rear bogies in Fig. 15(b)) of the lead locomotive. These two load cases ensured the x-axis symmetry did not double the loads on the bridge. ~~These load cases are shown in Table 4.~~ In the first load case, the three wheels of the front bogie were positioned on the arch such that the rear (third) wheel was at 3.5m (half of the 7m separation between the rear wheel of the front bogie and the first wheel of the second bogie) away from the arch centreline. In the second load case, the three wheels of the second bogie were positioned on the arch such that the rear (third) wheel was at 1.7m (half of the 3.4m separation between the rear wheel of the second bogie and the first wheel of the third bogie) away from the arch centreline.

The materials for masonry arch and soil fill were considered elastic since the field results showed very low strains which were in the elastic range. Masonry was modelled as a homogenised macro material as has been considered by many researchers (Janaraj and Dhanasekar 2014; Noor-E-Khuda et al. 2016 & 2018). Table 4 contains the properties of masonry and soil fill. The soil fill was modelled as wet/submerged soil which was evident from the field observations. For this purpose, 8 nodded 3D pore/fluid stress elements (C3D8P) were used to model the soil. The arch was meshed using 8 nodded 3D solid continuum elements (C3D8).

The interaction between the backfill and the masonry arch was simulated using the Mohr-Coulomb criterion to model the friction behaviour between the arch and the soil fill. The selected interface properties used in the FE model are shown in Table 5.

FE results

The minimum principal strain (maximum principal compressive strain) contours for the two load cases obtained from the FE analysis are shown in Fig. 21. Thrust line is also drawn in Fig. 21, which shows that when the load position changes, the thrust behaviour alters. The highest thrust strain observed was at the support for Load case II as can be observed in Fig. 21(b). The maximum tangential strains at all the three ROIs (crown, quarter point and support) were obtained from the FE analysis for the elements identified in Fig. 21 for both load cases.

The maximum tangential compressive strains measured from the FE analysis at the three ROIs and the corresponding field strains are presented in Table 6. The maximum difference between the FE and the field strains was 14.5% at the quarter point for case II which is reasonable for the magnitudes of the strain measured. It can, therefore, be inferred that the FE results confirm the field measurements for the considered load cases. The quarter modelling technique exploiting the x-axis and z-axis symmetries limited the load cases that could be considered; however, the two load cases provided sufficient insight into the response of the masonry arches to the positions of the wheel loads and provided confidence to the low levels of strains and deflection measured using the DIC method.

CONCLUSIONS

In this study, the deflections and strains were measured on two aged masonry arch bridges in Australia under the operating trains using DIC method. Data were measured over five nights on two bridges under 20 trains (10 passenger and 10 freight). Three ROIs (crown, quarter-point and support) on a selected arch of each bridge were imaged during the passage of the trains. The wheel positions, train lengths and speeds were ascertained using three lasers. The wheel position was shown as critical for the deflection and strain in the arch. A 3D micro FE model was formulated to validate the field strain magnitudes. Following conclusions have emerged from this research:

- DIC is a suitable method to measure deflection and strains on masonry arch rail bridges provided adequate care is taken to ensure the quality of images.
- Deflections and strains in masonry arch bridges can be quite low due to the structural form and the presence of the fill materials.
- Crown deflects consistently more than the other regions of interest in the arch. Under freight trains, the measured maximum radial deflections at crown of the Bridges 1 and 2 were 0.5mm and 0.24mm respectively.
- The measured absolute maximum strain was 110μ - well within the elastic limit as the ultimate strains in masonry.
- The train axle load position play important role to the variation of strains across the masonry arch.
- The laser data analysis showed that the deflection peaks corresponded well with the wheel positions. The determined time lag between the passage of first wheel across a ROI and the maximum deflection of the ROI was shown as a function of the train speed.

- FE analysis results validated the field strains; the strain magnitudes and the strain variation trends agreed well with the field data. The effect of train wheel position on the strain variation was verified for two selected load cases.

Acknowledgments

The authors gratefully acknowledge the funding provided by the ARTC Chief Executive Officer, John Fullerton, to conduct this research.

REFRENCES

Acikgoz, S., DeJong, M.J., Kechavarzi, C., Soga, K. (2018) "Dynamic response of a damaged masonry rail viaduct: Measurement and interpretation", *Engineering Structures*, 168, 544-558.

Alani, M. A., Aboutalebi, M. and Kilic, G. (2013), "Applications of ground penetrating radar (GPR) in bridge deck monitoring and assessment", *Journal of Applied Geophysics,* 97 (2013) 45–54.

Askarinejad, H., Dhanasekar, M., and Cole, C.R. (2013) "Assessing the effects of track input on the response of insulated rail joints using field experiments", *Proc Institution of Mechanical Engineers, Part F: Journal of Rail and Rapid Transit*, 227 (2), 176-187.

Ataei, S., Miri, A. and Jahangiri, M. (2017). "Assessment of load carrying capacity enhancement of an open spandrel masonry arch bridge by dynamic load testing", *International Journal of Architectural Heritage,* 8, 1086–1100.

Audenaert, A., and Beke, J. (2010). "A comparison between 2D-models for masonry arch bridge assessment", *Proc., 3rd WSEAS International Conference on Engineering Mechanics, Structures, and Engineering Geology,* Corfu Island, Greece, 251-256.

Baldi, A. (2018). "Digital Image Correlation and Color Cameras", *Experimental Mechanics* 58:315–333

Bandula Heva, T., Dhanasekar, M., and Boyd, P. (2013) Experimental investigation of wheel/rail rolling contact at railhead edge, *Experimental Mechanics*, 53 (6), 943-957.

Bandula Heva, T., and Dhanasekar, M. (2014) Failure of discontinuous railhead edges due to plastic strain accumulation, *Engineering Failure Analysis*, 44, 110-124.

Busca, G., Cigada, A., Mazzoleni, P. and Zappa, E. (2014). “Vibration Monitoring of Multiple Bridge Points by Means of a Unique Vision-Based Measuring System”, Experimental Mechanics, 54, 255–271

Callaway, P., Smith, C. C., and Gilbert, M. (2012). “Influence of backfill on the capacity of masonry arch bridges.” *Proceedings of the Institution of Civil Engineers (Bridge Engineering),* 165, 147-158.

Dhanasekar, M., and Bayissa, W. (2011a). “Structural adequacy assessment of a disused flat bottom rail wagon as road bridge deck.” *Engineering Structures,* 33(5), 1838-1849.

Dhanasekar, M. and Bayissa, W. (2011b). “Performance of square and inclined insulated rail joints based on field strain measurements”, *Proc. IMechE Part F: J. Rail and Rapid Transit* (226), 140-154.

Dhanasekar, M., Thamboo, J.A. and Nazir, S. (2017), On the in-plane shear response of the high bond strength concrete masonry, *Materials and Structures*, 50(5), DOI 10.1617/s11527-017-1078-7

Feng, D.M., Feng, M.Q., Ozer, E. and Fukuda, Y. (2015). “A Vision-Based Sensor for Noncontact Structural Displacement Measurement”, *Sensors*, 15, 16557-16575

Forsey, A. and Gungor, S. (2016) Demosaicing images from colour cameras for digital image correlation, *Optics and Lasers in Engineering*, 86, 20-28

Ghorbani, R., Matta, F., and Sutton, M.A. (2015). “Full-Field Deformation Measurement and Crack Mapping on Confined Masonry Walls Using Digital Image Correlation.” *Experimental Mechanics*, 55, 227–243.

Harvey, W. J. (1988). "Application of the mechanism analysis to masonry arches." *The Structural Engineer*, 66(5), 77–84.

Hulet, K. M., Smith, C. C., and Gilbert, M. (2006). "Load-carrying capacity of flooded masonry arch bridges." *Proc of the Inst of Civil Engineers (Bridge Engineering),* 159, 97-103.

ISTRA4D Software Manual. (2016). Q-400 System, Dantec Dynamics, version 4.4.5 v1, Nova Instruments Company, Germany.

Jamtsho, L., and Dhanasekar, M. (2013). "Performance testing of a road bridge deck containing flat rail wagons." *Journal of Bridge Engineering ASCE*, 18(4), 308-317.

Janaraj, T., and Dhanasekar, M. (2014). "Finite element analysis of the in-plane shear behaviour of masonry panels confined with reinforced grouted cores." *Construction and Building Materials,* 65, 495–506.

Kishen, J. M. C., Ramaswamy, A., and Manohar, C. S. (2013). "Safety Assessment of a Masonry Arch Bridge: Field Testing and Simulations." *Journal of Bridge Engineering ASCE*, 18(2), 162-171.

Koltsida, I., Tomor, A., and Booth, C. (2013). "The use of digital image correlation technique for monitoring masonry arch bridges." *Proc., 13th Intl Conf on Arch Bridges, ARCH 13*, Split, Croatia, 2-4 October 2013.

Lee, J., Oh, J., Park, M., Kwon S., and Kwark, J. (2006). "Bridge displacement measurement system using image processing." *Proc., IABMAS'06 – Bridge maintenance, safety, management, resilience and sustainability*. Porto, Portugal.

Li, J.R., Dan, X.Z., Wang, Y.H., Yang, G.B and Yang, L.X. (2017). "3D digital image correlation using single color camera pseudo-stereo system", *Optics and Laser Tech.*, 95, 1-7.

Ling, L., Dhanasekar, M. and Thambiratnam, D.P. (2018). “Dynamic response of train–track–bridge system subjected to derailment impacts”, Vehicle System Dynamics, 56(4), 638-57.

Malesa, M., Szczepanek, D., Kujawińska, M., Świercz, A., and Kołakowski, P. (2010). “Monitoring of civil engineering structures using Digital Image Correlation technique.” *Proc., 14th Int Conf on Experimental Mechanics (ICEM 14).* Poitiers, France.

Melbourne, C. (2008). “Design of Arch Bridges.” *ICE manual of Bridge Engg*, ICE Manuals.

Murray, C.A., Take, W.A. and Hoult, N.A. (2014). “Measurement of vertical and longitudinal rail displacements using digital image correlation”, *Can. Geotech. J.* 52: 141–155

Noor-E-Khuda, S., and Dhanasekar, M. (2018). “Masonry Walls under Combined In-Plane and Out-of-Plane Loadings.” *Journal of Structural Engineering*, 10.1061/(ASCE)ST.1943-541X.0001930, 04017186.

Noor-E-Khuda, S., Dhanasekar, M., and Thambiratnam, D. P. (2016). “An explicit finite element modelling method for masonry walls under out-of-plane loading.” *Engineering Structures*, 113, 103–120.

Orban, Z., and Gutermann, M. (2009). “Assessment of masonry arch railway bridges using non-destructive in-situ testing methods.” *Engineering Structures*, 31, 2287-2298.

Pan, B., Qian, K., Xie, H., Asundi, A. (2009). “Two-dimensional digital image correlation for in-plane displacement and strain measurement: a review.” *Measurement Science and Technology*, 20, 1-17.

Papaelias, M.Ph., Roberts, C., and Davis, C.L. (2008) “A review on non-destructive evaluation of rails: state-of-the-art and future development”, Proc. IMechE Part F: J. Rail and Rapid Transit, 222, 367-384

Ramos, T., Furtado, A., Eslami, S., Alves, S., Rodrigues, H., Arêde, A., Tavares, P. J., and Moreira, P. M. G. P. (2015). “2D and 3D Digital Image Correlation in Civil Engineering – Measurements in a Masonry Wall.” *Procedia Engineering,* 114, 215 – 222.

Ribeiro, D., Calçada, R., Ferreira, J., and Martins, T. (2014). “Non-contact measurement of the dynamic displacement of railway bridges using an advanced video-based system.” *Engineering Structures*, 75, 164–180.

Sabato, A and Niezrecki, C. (2017) “Feasibility of digital image correlation for railroad tie inspection and ballast support assessment’, Measurement, 103, 93-105

Savitzky, A., and Golay, M.J.E. (1964). “Smoothing and Differentiation of Data by Simplified Least Squares Procedures.” *Analytical Chemistry*, 36 (8), 1627-1639.

Srinivas, V., Sasmal, S., Ramanjaneyulu, K., and Ravisankar, K. (2014). “Performance Evaluation of a Stone Masonry–Arch Railway Bridge under Increased Axle Loads.” *Journal of Performance of Constructed Facilities, ASCE,* 28(2), 363-375.

Standard Australia. (2017). “Bridge Design Loads.” *AS5100.2*, Sydney, Australia.

Standard Australia. (2018). “Masonry Structures.” *AS3700*, Sydney, Australia.

Thamboo, J.A., and Dhanasekar, M. (2015). “Characterisation of thin layer polymer cement mortared concrete masonry bond.” *Construction and Building Materials*, 82, 71–80.

Thamboo, J.A., Dhanasekar, M., and Cheng, Y. (2013a). “Effects of joint thickness adhesion and web shells to the face shell bedded concrete masonry loaded in compression.” *Australian Journal of Structural Engineering*; 14(3), 291-302.

Thamboo, J.A., Dhanasekar, M., and Cheng, Y. (2013b). "Flexural and shear bond characteristics of thin layer polymer cement mortared concrete masonry." *Construction and Building Materials*, 46, 104–113.

Tung, S. H., Shih, M.H., and Sung, W.P. (2008). "Development of digital image correlation method to analyse crack variations of masonry wall." *Sadhana*, 33(6), 767–779.

White, D.J., Take, W.A. & Bolton, M.D. (2003). "Soil deformation measurement using particle image velocimetry (PIV) and photogrammetry." *Geotechnique*, 53, 619-631.

Zahra, T., and Dhanasekar, M. (2016). "A generalised damage model for masonry under compression." *International Journal of Damage Mechanics*, 25(5), 629–660.

Zahra, T., and Dhanasekar, M. (2018). "Characterisation and strategies for mitigation of the contact surface unevenness in dry-stack masonry." *Construction and Building Materials*, 169, 612–628.

Zong, N., Askarinejad, H., Bandula Heva, T., and Dhanasekar, M. (2013) Service condition of railroad corridors around the insulated rail joints, Journal of Transportation Engineering, ASCE, 139 (6), 643-650.

Zong, N., and Dhanasekar, M. (2014) Experimental studies on the performance of rail joints with modified wheel/railhead contact, *Proc. Inst Mech Engineers, Part F: Journal of Rail & Rapid Transit*, 228 (8), 857-877

Fig. 1. Selected arch for investigation (a) Bridge – 1 (b) Bridge – 2

Fig. 2. Selected regions of interest for measurement (a) Bridge – 1 (b) Bridge – 2

Fig. 3. Instrumentation for field measurements

Fig. 4. *ISTRA4D* Analysis Process

Fig. 5. Results extraction from *ISTRA4D*

Fig. 6. Noise levels in data with and without filter

Fig. 7. Radial deflections – Bridge 1; Passenger Train

Fig. 8. Radial deflections – Bridge 2; Passenger Train

Fig. 9. Radial deflections – Bridge 1; Freight Train

Fig. 10. Radial deflections – Bridge 2; Freight Train

Fig. 11. Tangential strains – Bridge 1; Passenger Train

Fig. 12. Tangential strain – Bridge 2; Passenger Train

Fig. 13. Peak radial strain – for Bridges 1 and 2

Fig. 14. Typical laser signals for train wheel passing

Fig. 15. Typical wheel positions and train lengths

Fig. 16. Wheel positions and crown deflection peaks (Passenger train)

Fig. 17. Wheel positions and crown deflection peaks (Freight train)

Fig. 18. Variation of tangential strains across ROIs with wheel positions

Fig. 19. 3D FE Model of bridge arch with backfill

Fig. 20. Description of bridge width considered in modelling

Fig. 21. Principal (compressive) strain from FE model for different load cases

(a) (b)

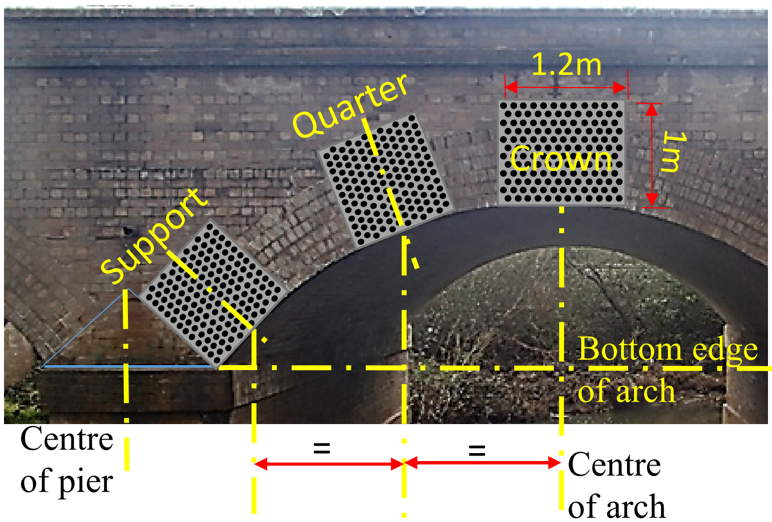

1.2m
1m
Quarter
Crown
Support
Bottom edge
of arch
Centre
of pier
=
=
Centre
of arch

(a)

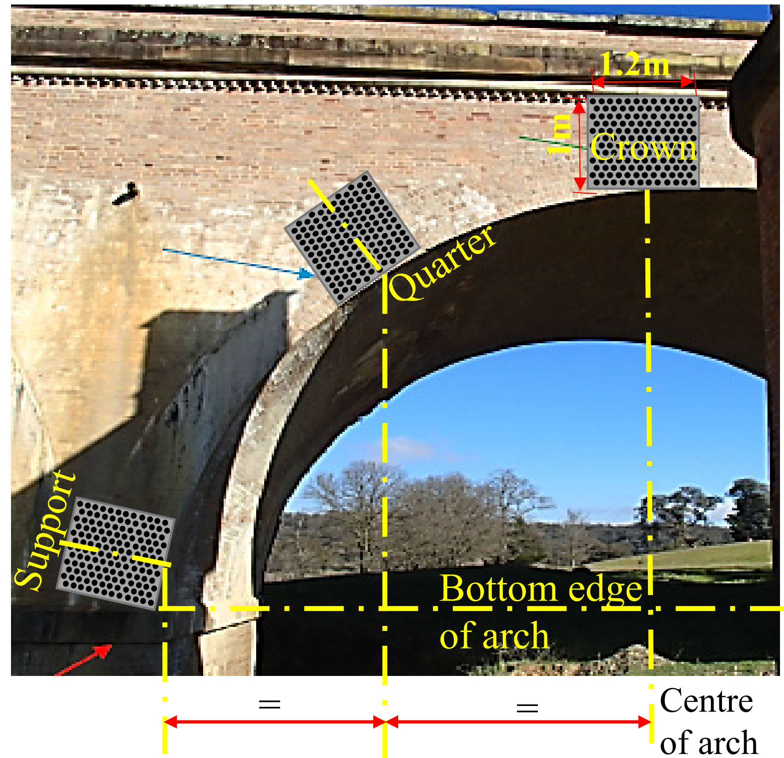

1.2m
1m
Crown
Quarter
Support
Bottom edge
of arch
=
=
Centre
of arch

(b)

(a) Cleaning of ROIs

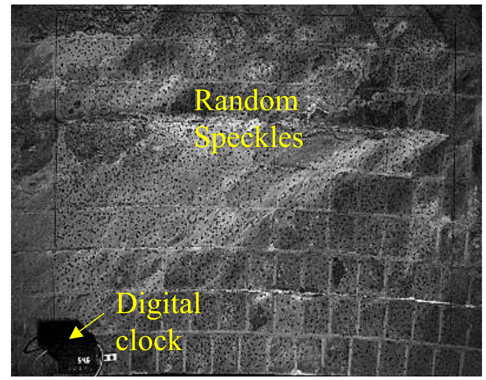

(b) Speckling of ROIs

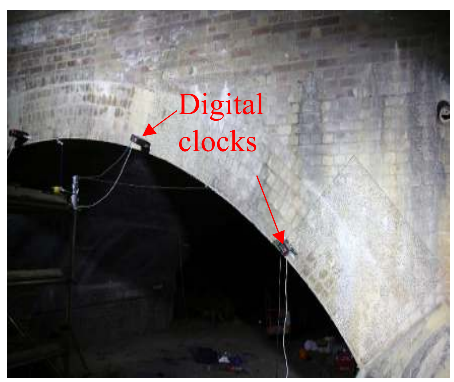

(c) Prepared ROIs

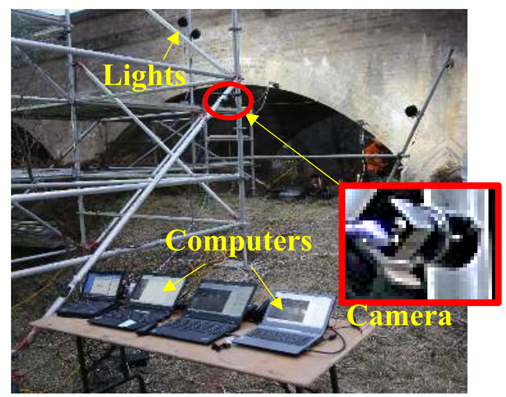

(d) Digital Image Recording

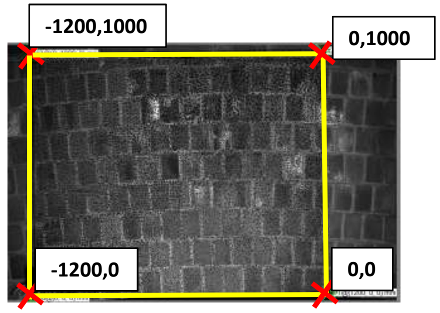

(a) Calibration

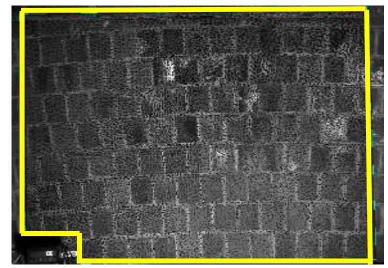

(b) Measurement area selection

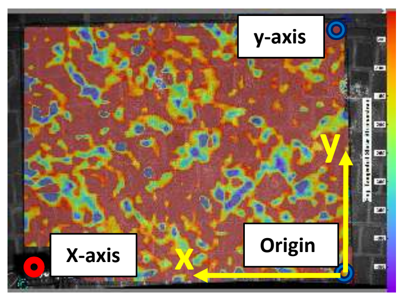

(c) Reference coordinates definition

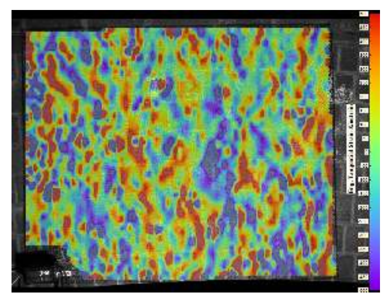

(d) Tangential strain distribution

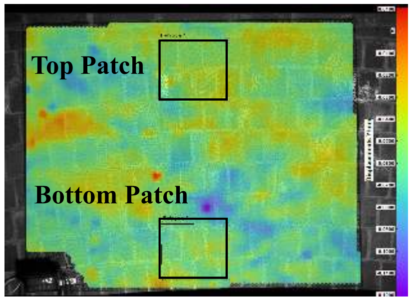

(a) Selection of patches
in top & bottom of ROI

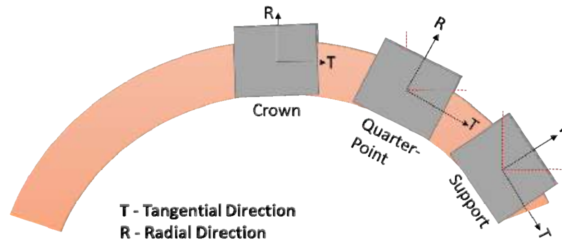

(b) ROIs for Bridge 1

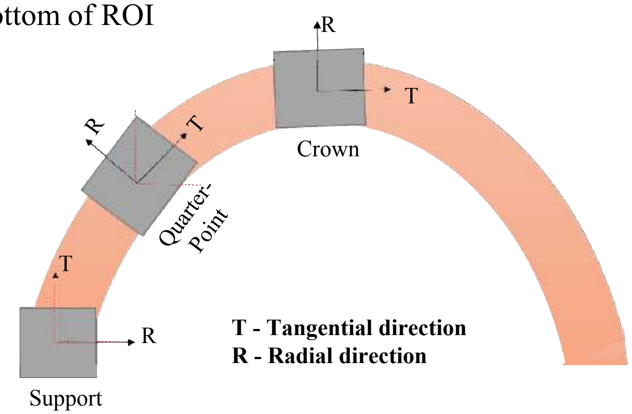

(c) ROIs for Bridge 2

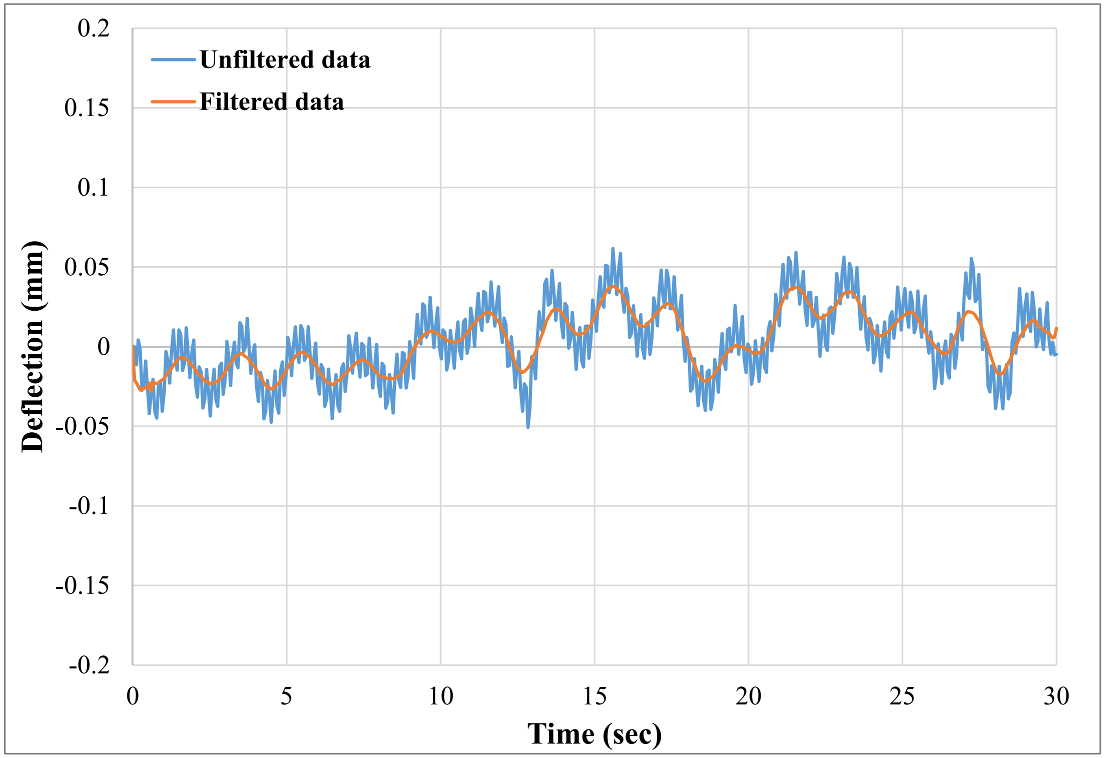
Unfiltered data
Filtered data
0.2
0.15
0.1
0.05
0
-0.05
-0.1
-0.15
-0.2
Deflection (mm)
0
5
10
15
20
25
30
Time (sec)

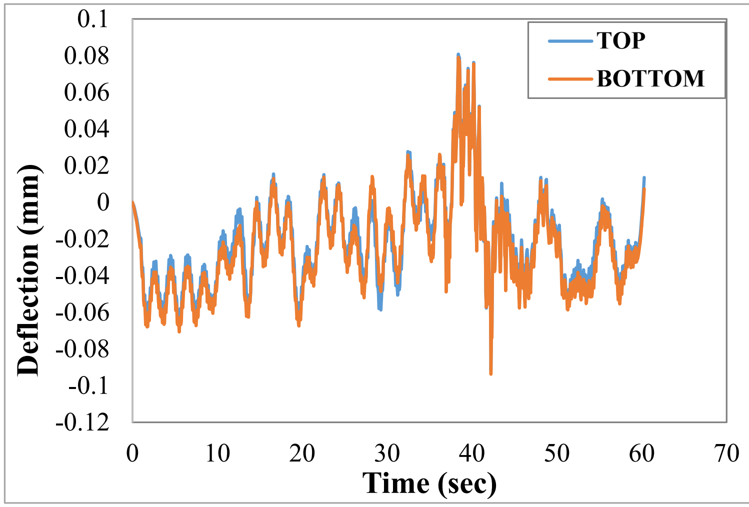

(a) Crown

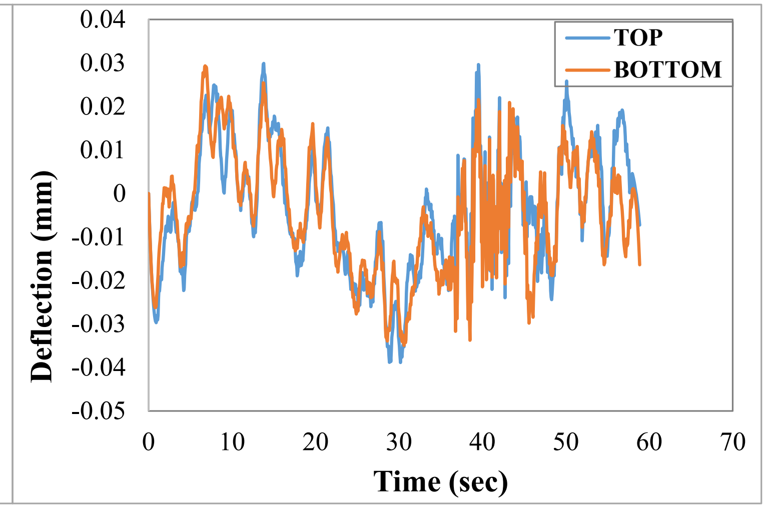

(b) Quarter-Point

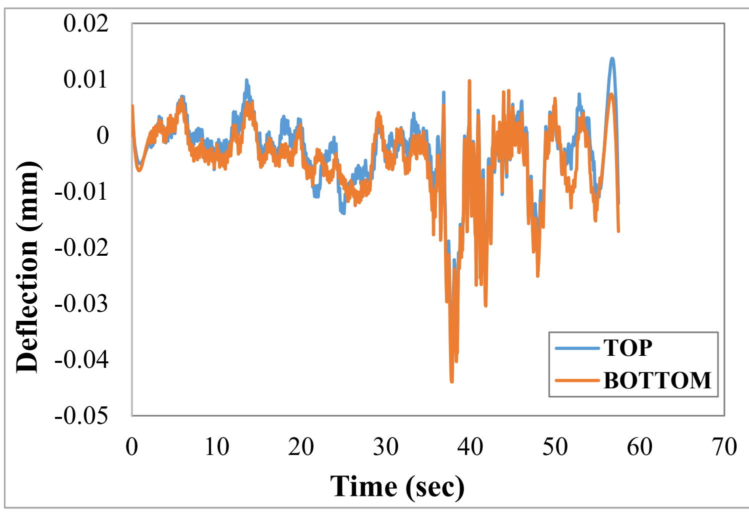

(c) Support

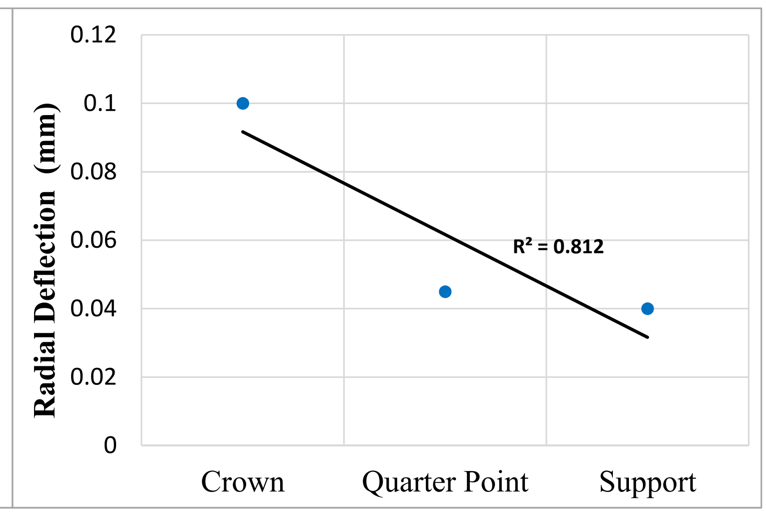

(d) Variation of peak deflection

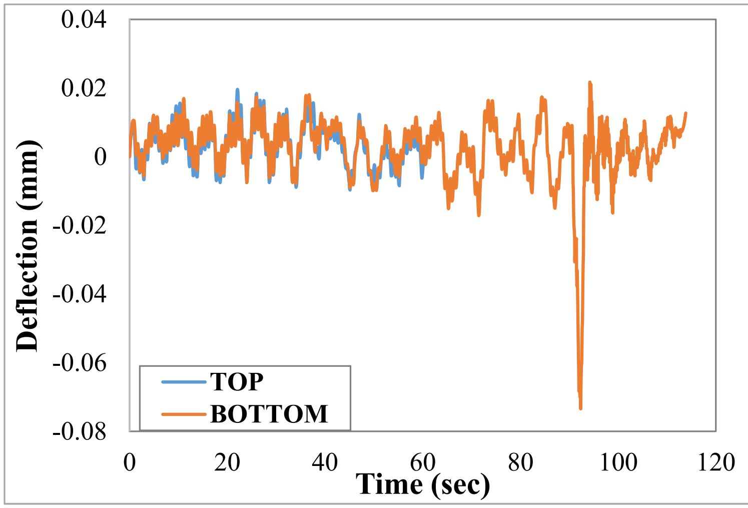

(a) Crown

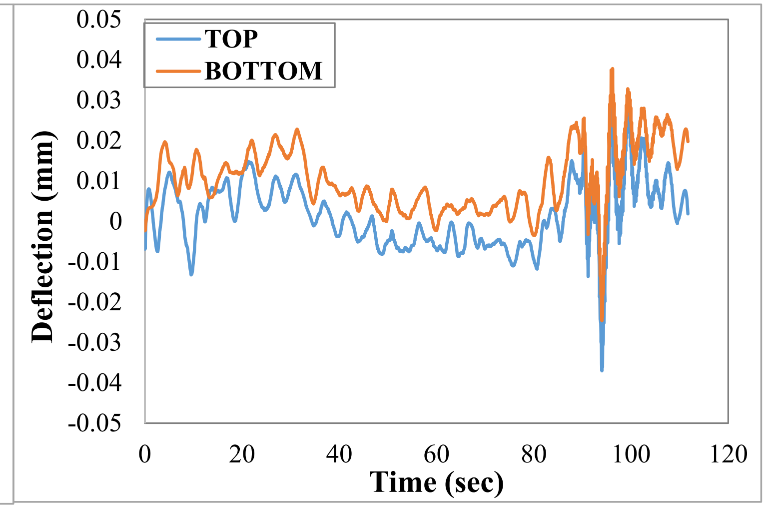

(b) Quarter-Point

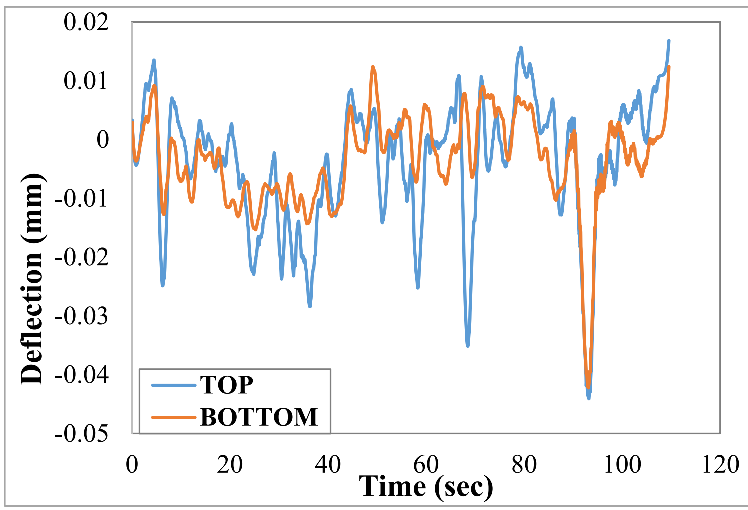

(c) Support

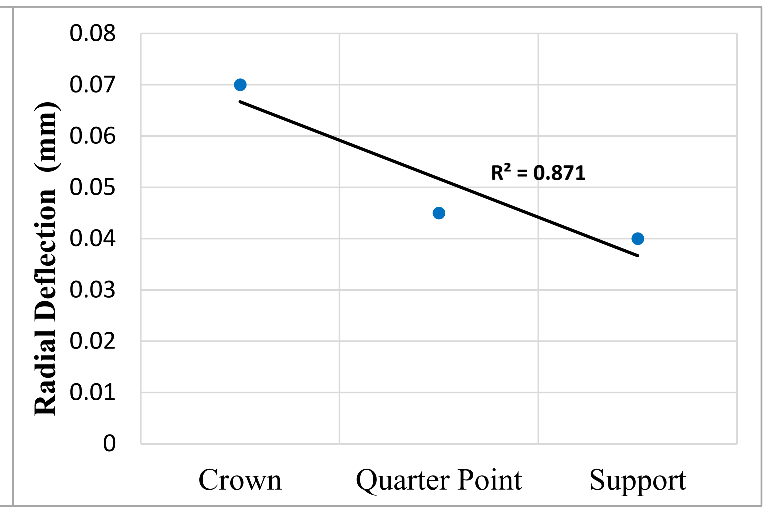

(d) Variation of peak radial deflection

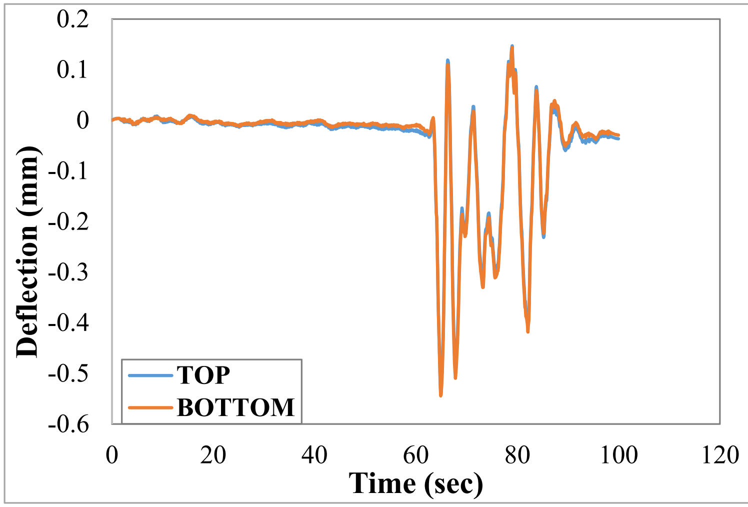

(a) Crown

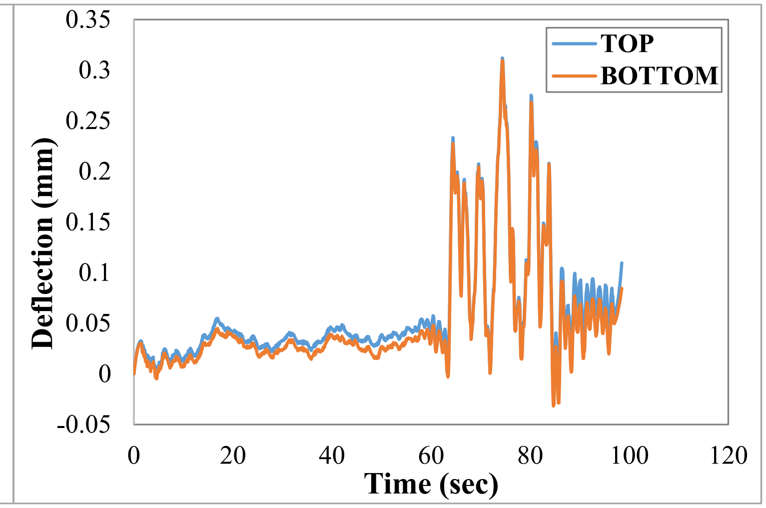

(b) Quarter-Point

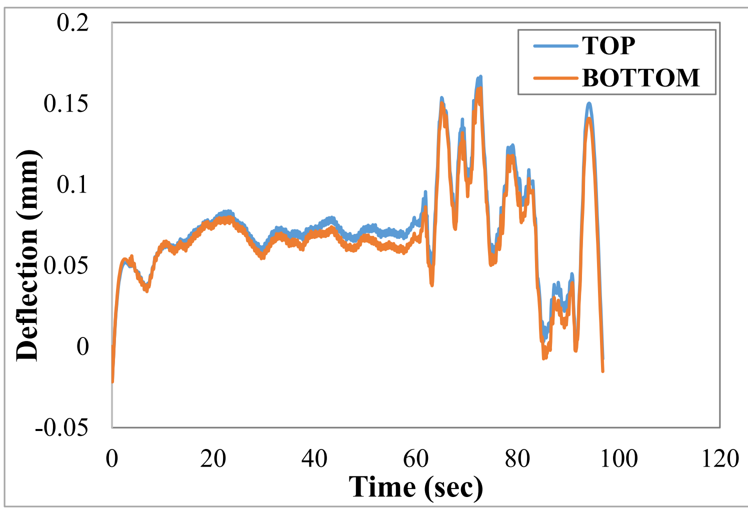

(c) Support

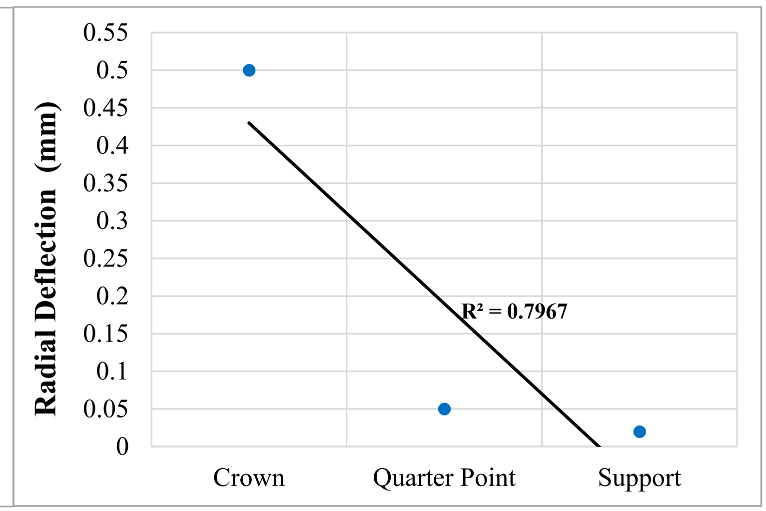

(d) Variation of peak radial deflection

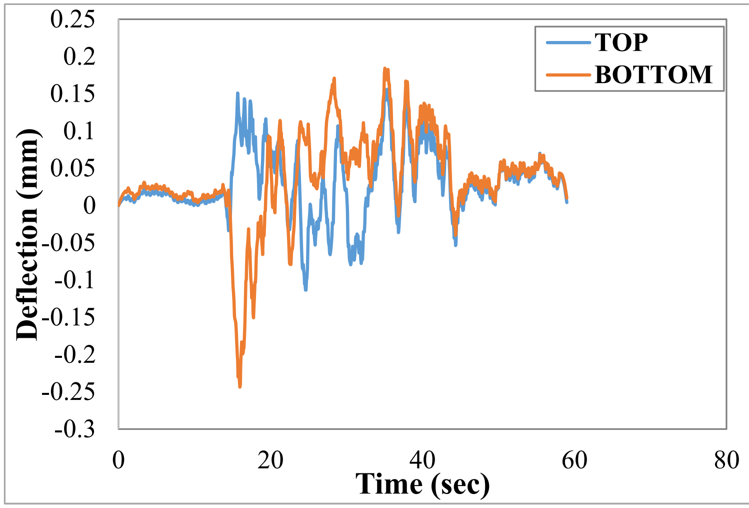

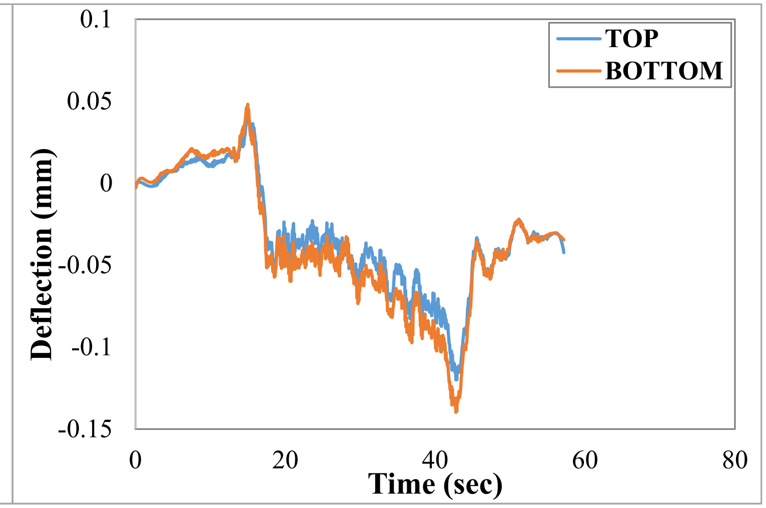

(a) Crown

(b) Quarter-Point

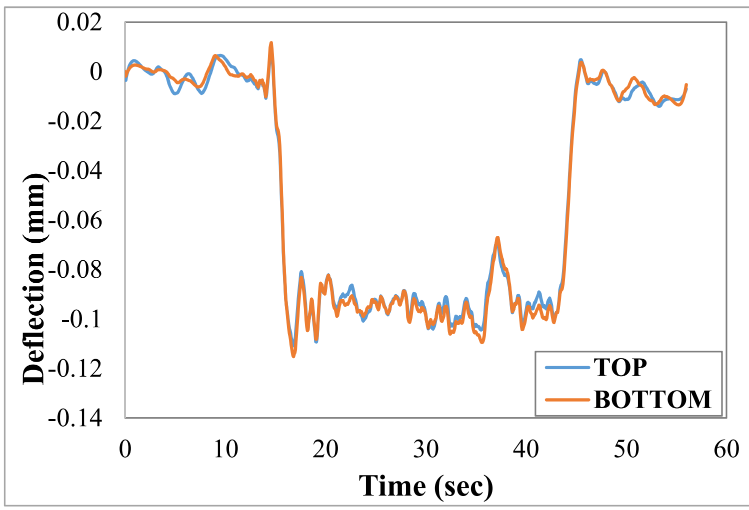

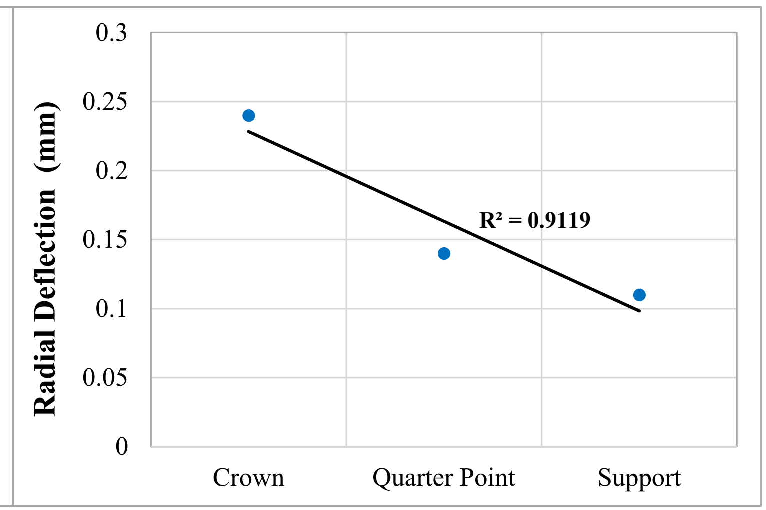

(c) Support

(d) Variation of peak radial deflection

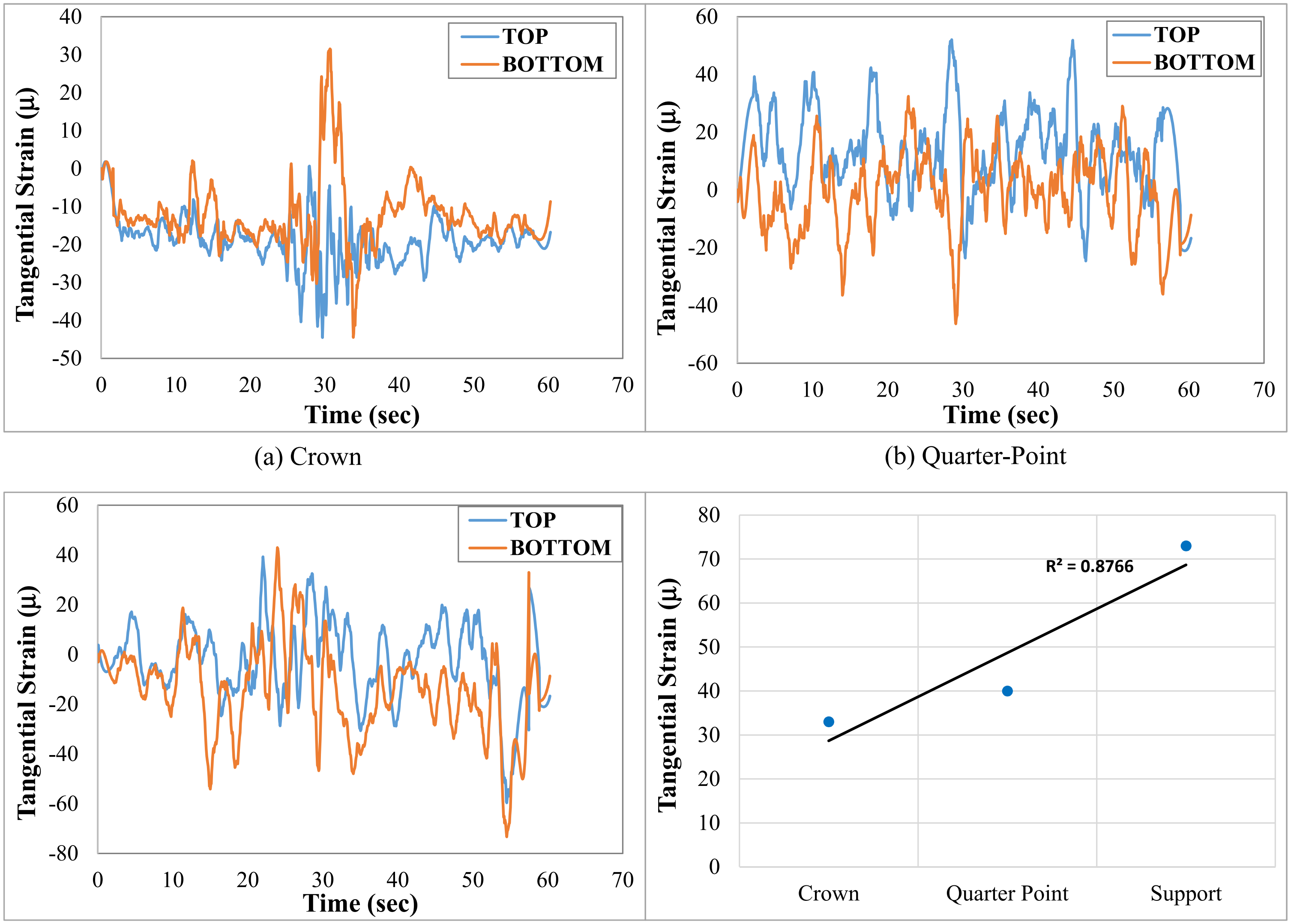

(a) Crown

(b) Quarter-Point

(c) Support

(d) Variation of peak tangential strain

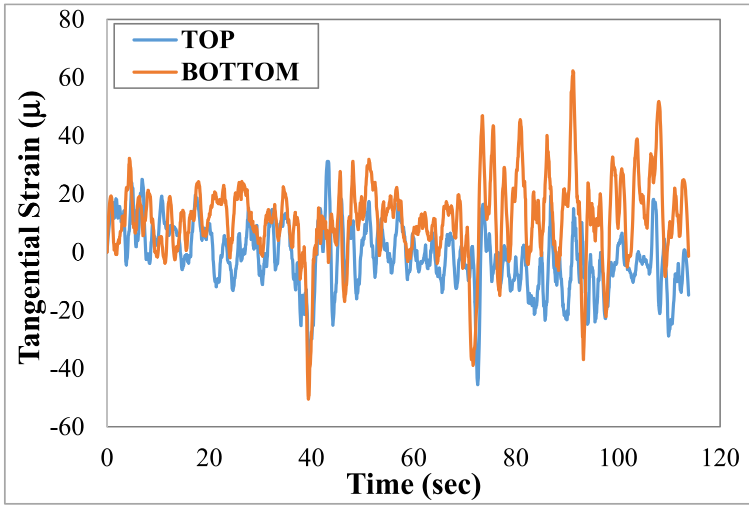

(a) Crown

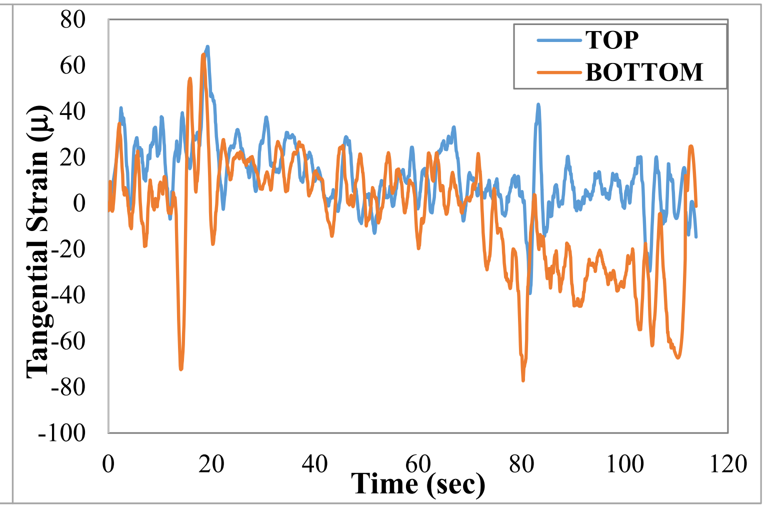

(b) Quarter-Point

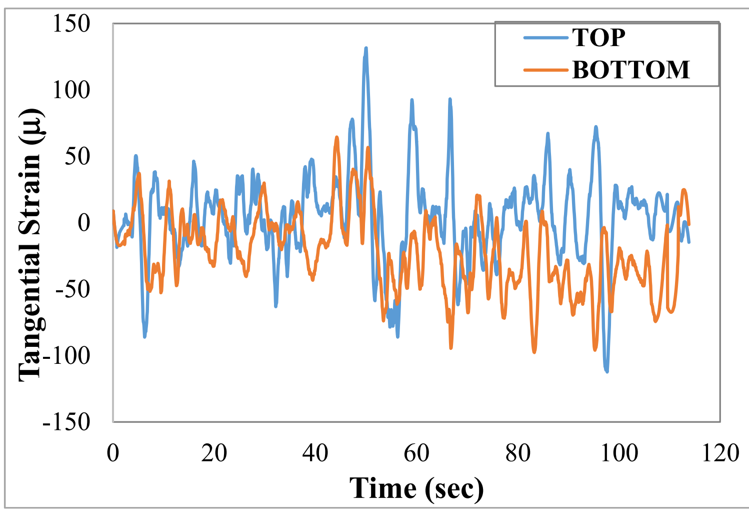

(c) Support

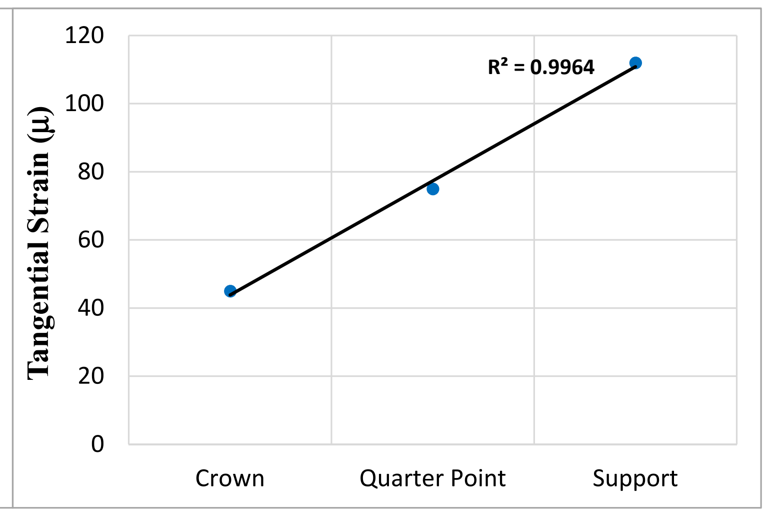

(d) Variation of peak tangential strain

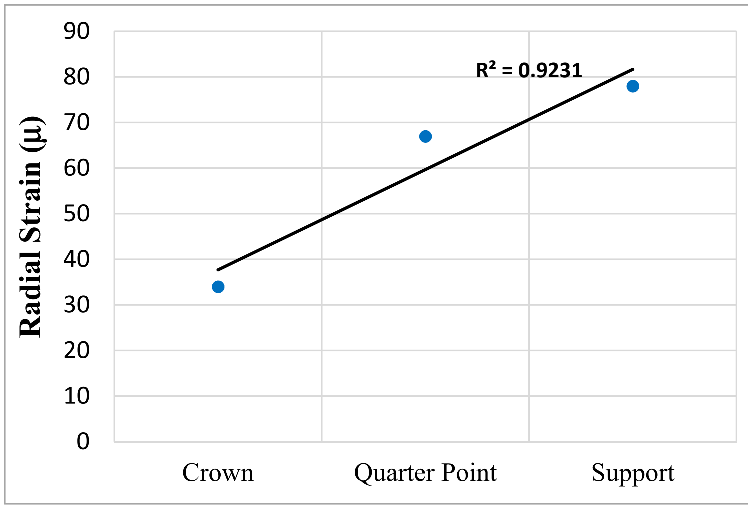

(a) For a passenger train (Bridge 1)

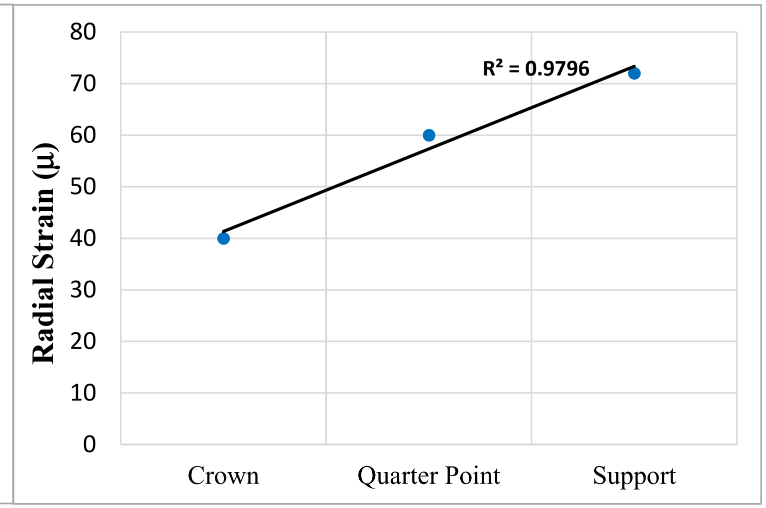

(b) For a freight train (Bridge 1)

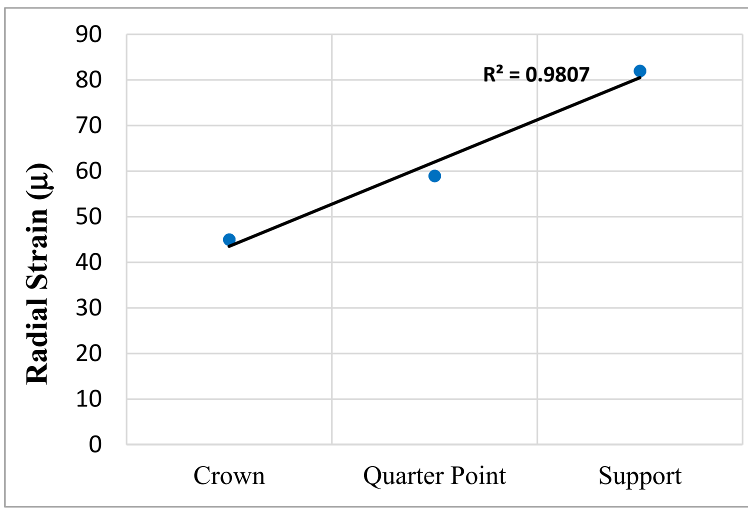

(c) For a passenger train (Bridge 2)

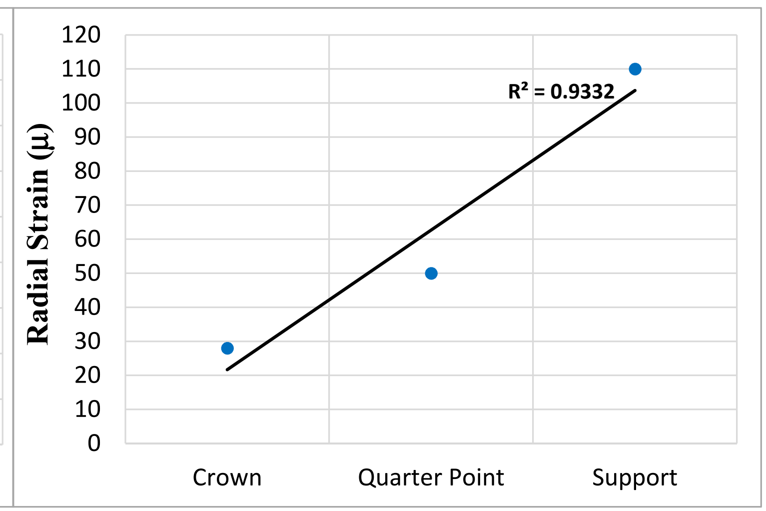

(d) For a freight train (Bridge 2)

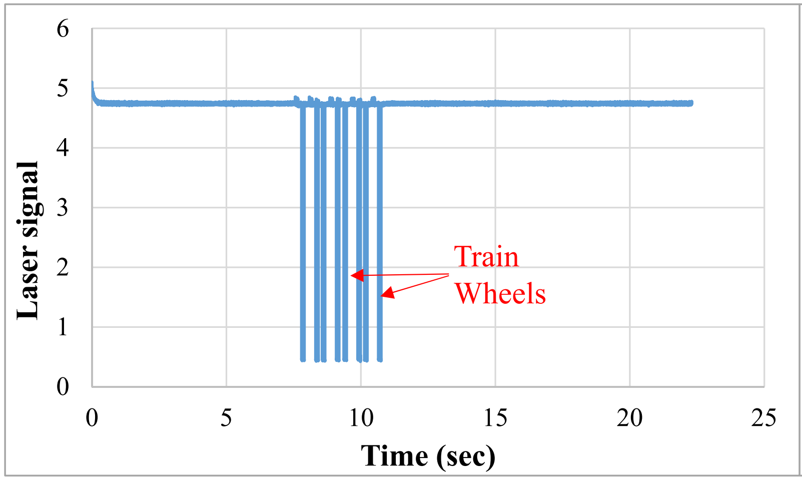

(a) For a passenger train

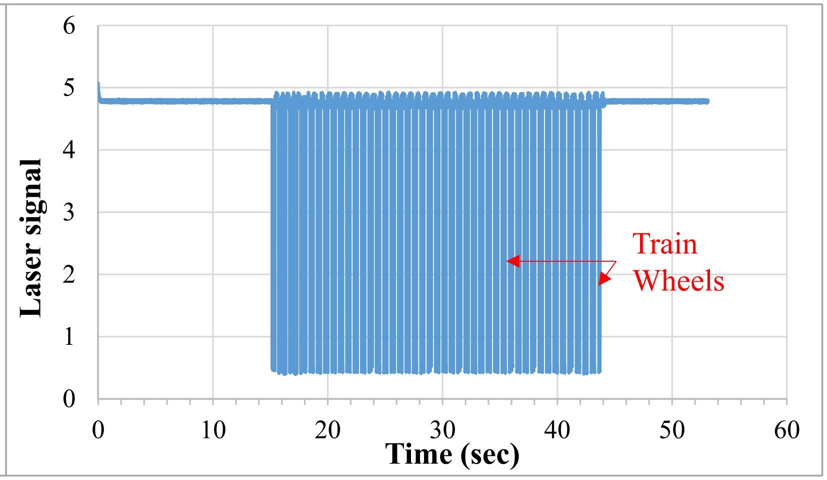

(b) For a freight train

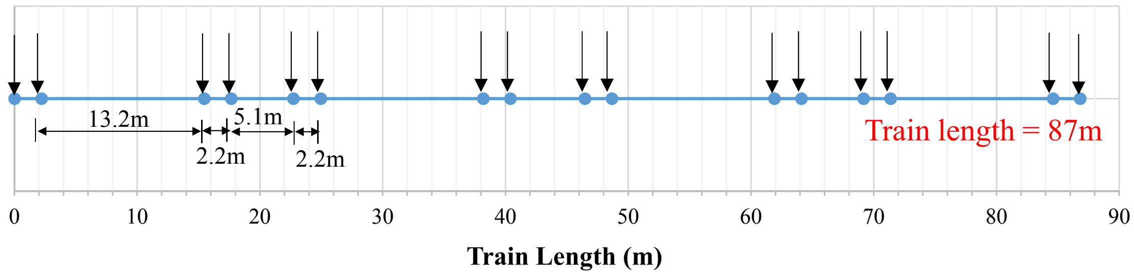

(a) For a typical passenger train

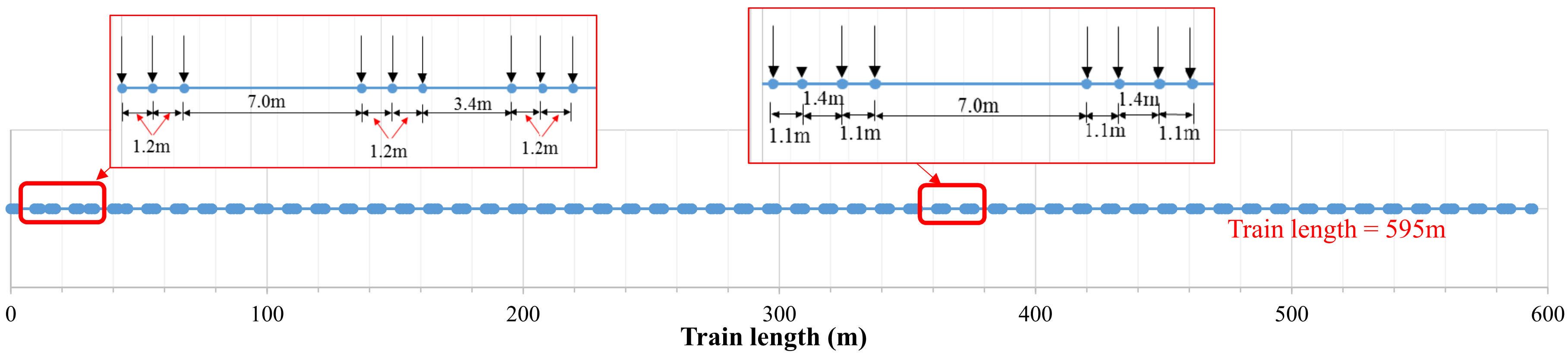

(b) For a typical freight train

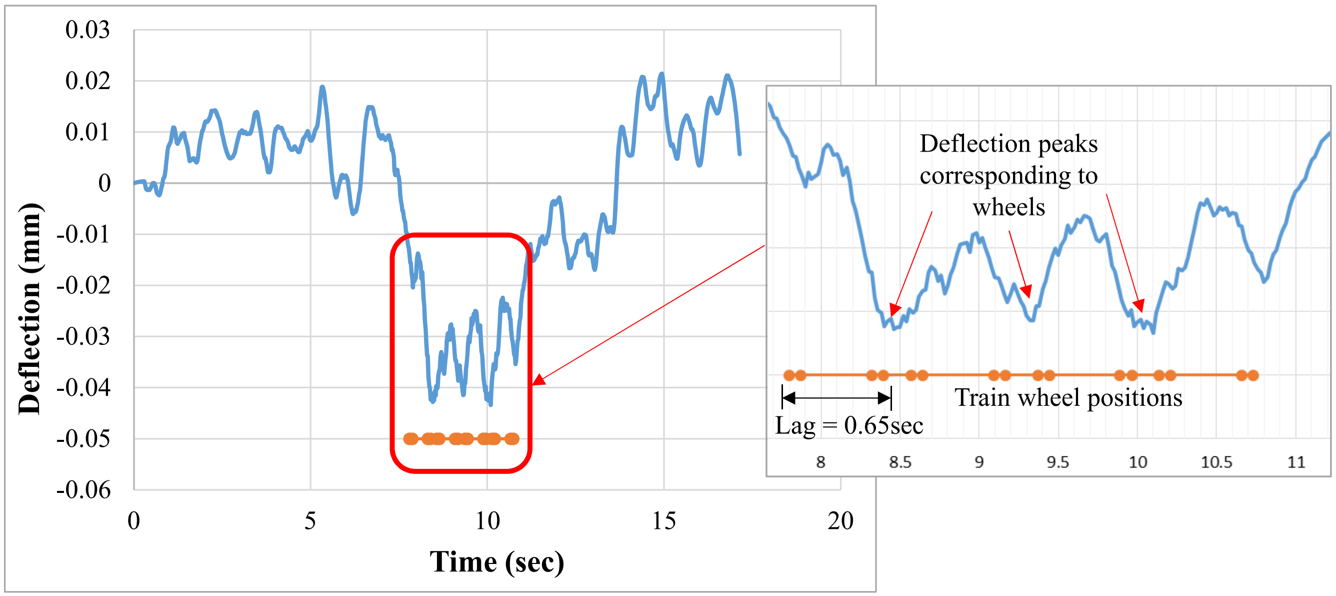

0.03
0.02
0.01
0
-0.01
-0.02
-0.03
-0.04
-0.05
-0.06
Deflection (mm)
0
5
10
15
20
Time (sec)
Deflection peaks
corresponding to
wheels
Train wheel positions
Lag = 0.65sec
8
8.5
9
9.5
10
10.5
11

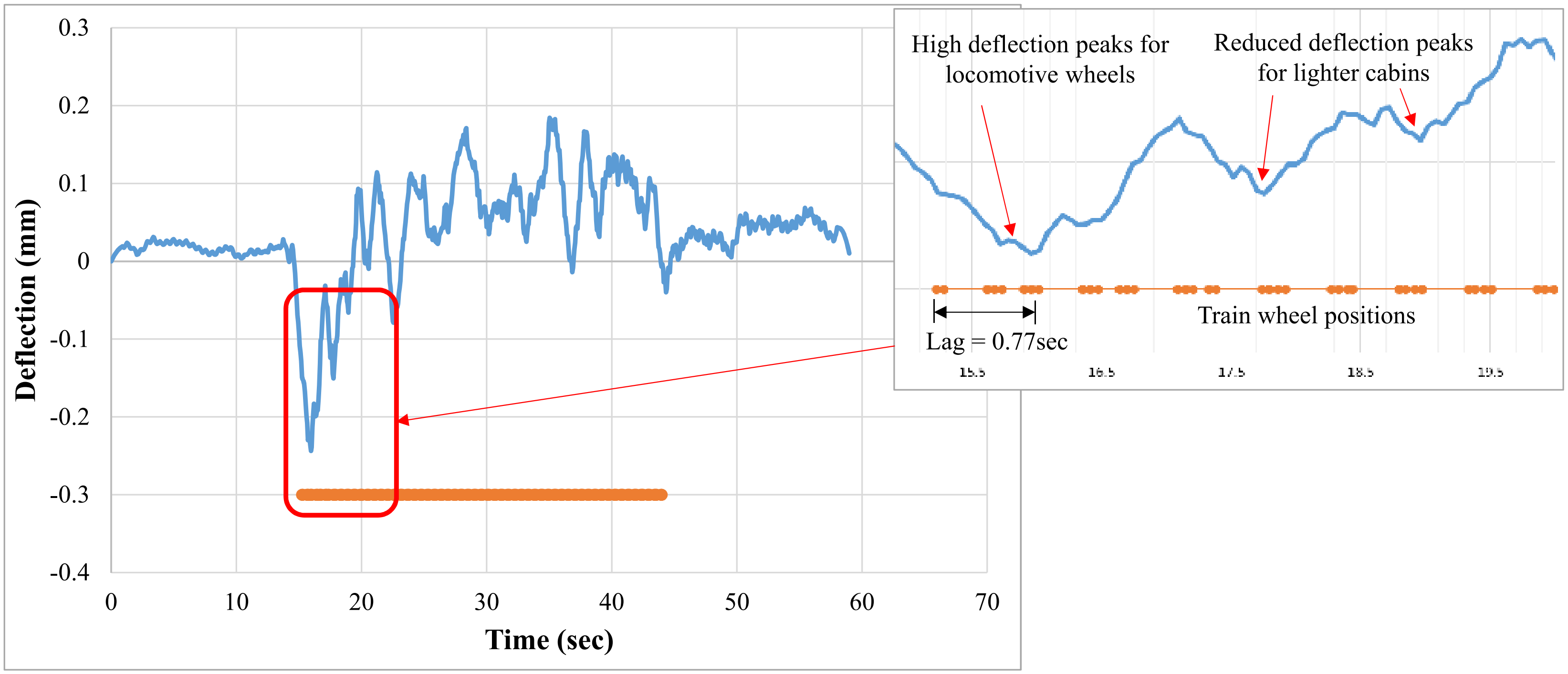
0.3
0.2
0.1
0
-0.1
-0.2
-0.3
-0.4
Deflection (mm)
0
10
20
30
40
50
60
70
Time (sec)
High deflection peaks for locomotive wheels
Reduced deflection peaks for lighter cabins
Train wheel positions
Lag = 0.77sec
15.5
16.5
17.5
18.5
19.5

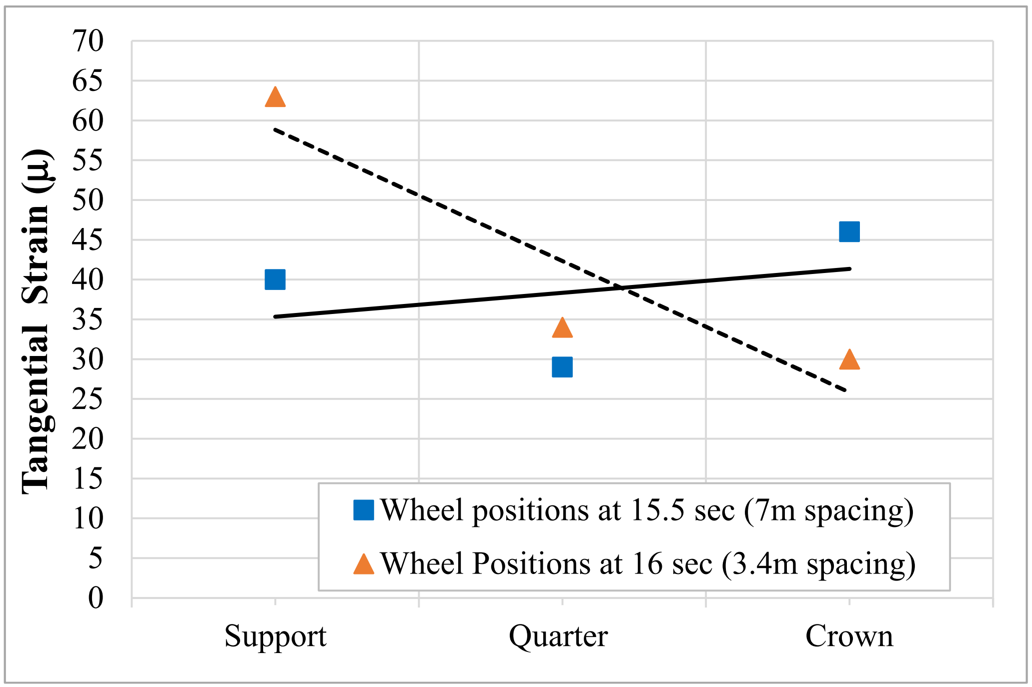
Tangential Strain (μ)
70
65
60
55
50
45
40
35
30
25
20
15
10
5
0
Support
Quarter
Crown
Wheel positions at 15.5 sec (7m spacing)
Wheel Positions at 16 sec (3.4m spacing)

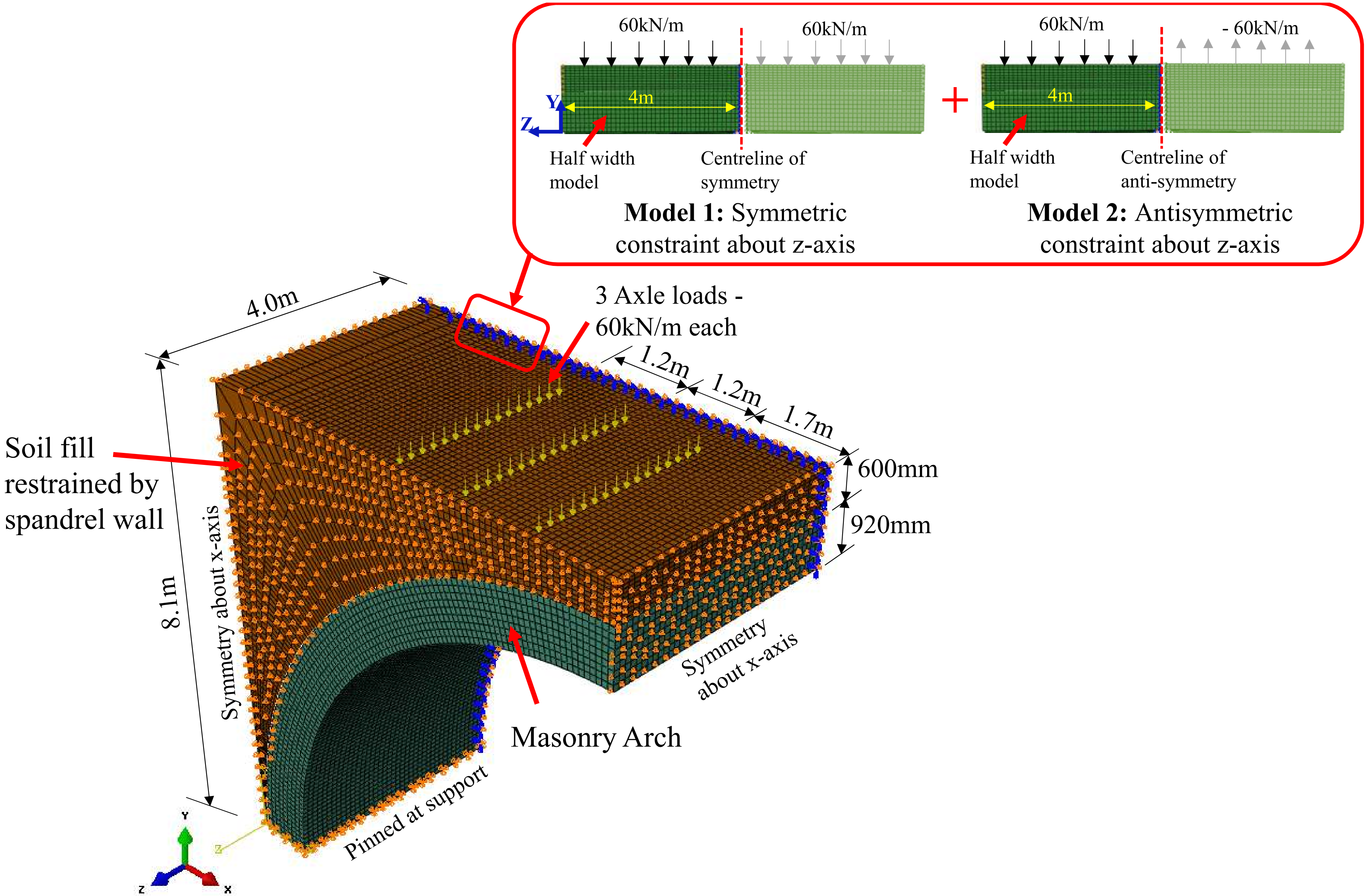
60kN/m
60kN/m
4m
Y
Z
Half width model
Centreline of symmetry
Model 1: Symmetric constraint about z-axis
+
60kN/m
- 60kN/m
4m
Half width model
Centreline of anti-symmetry
Model 2: Antisymmetric constraint about z-axis
4.0m
3 Axle loads - 60kN/m each
1.2m
1.2m
1.7m
600mm
920mm
Soil fill restrained by spandrel wall
8.1m
Symmetry about x-axis
Symmetry about x-axis
Masonry Arch
Pinned at support

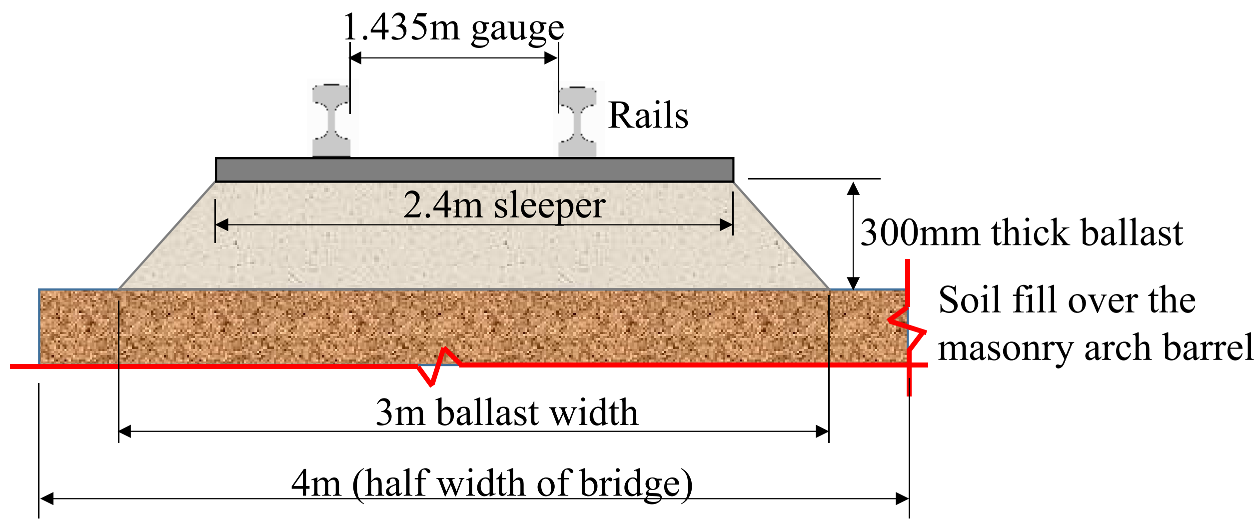
1.435m gauge
Rails
2.4m sleeper
300mm thick ballast
Soil fill over the
masonry arch barrel
3m ballast width
4m (half width of bridge)

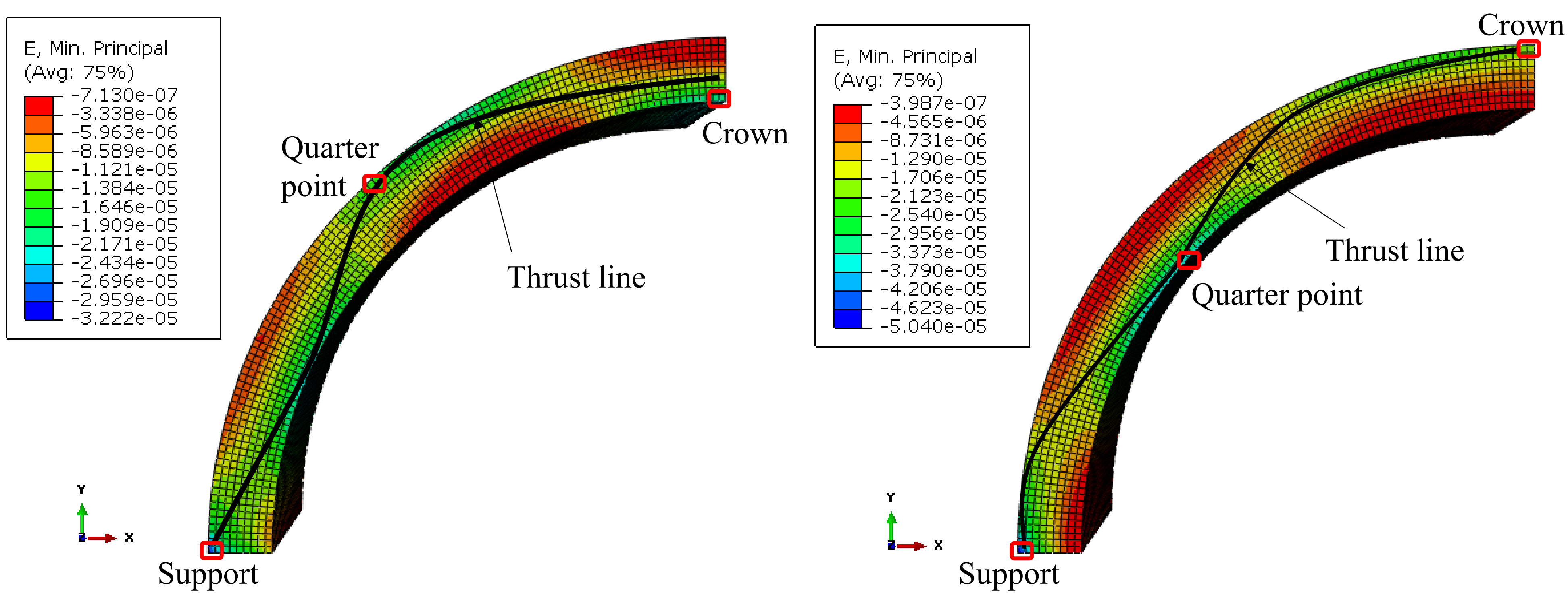

(a) Load case I

(b) Load case II